



## Inverse design of compounds that have simultaneously ferroelectric and Rashba cofunctionality

Carlos Mera Acosta <sup>1,2,\*</sup>, Adalberto Fazzio,<sup>3</sup> Gustavo M. Dalpian,<sup>2</sup> and Alex Zunger <sup>1,†</sup><sup>1</sup>Renewable and Sustainable Energy Institute, University of Colorado, Boulder, Colorado 80309, USA<sup>2</sup>Center for Natural and Human Sciences, Federal University of ABC, Santo Andre, São Paulo, Brazil<sup>3</sup>Brazilian Nanotechnology National Laboratory CNPEM, 13083-970, Campinas, São Paulo, Brazil

(Received 10 June 2020; accepted 24 August 2020; published 14 October 2020)

Cofunctionality—the coexistence of different (possibly even contraindicated) properties in the same compound—is an exciting prospect that never fails to deliver interesting surprises, as in transparent while electrically conducting compounds, topological insulators having Rashba spin split bands, or electrically conducting while thermally insulating (thermoelectric) compounds. Here we study a cofunctionality of ferroelectricity and Rashba effect that combines the directional helical *spin*-polarization characteristic of the energy bands of bulk Rashba compounds with the existence of two opposite electric polarization states, characteristic of *atomic* displacements in displacive ferroelectrics. Flipping of the ferroelectric polarization (e.g., via an applied electric field) would result in the reversal of the Rashba spin polarization. However, thus far, only very few (essentially one) compounds have been found to be ferroelectric Rashba semiconductors (FERSCs), e.g., GeTe (*R3m*). In this paper, we propose a general strategy for the identification of compounds that possess cofunctionalities and apply it to perform an inverse design, finding compounds that simultaneously have ferroelectricity and Rashba spin splitting. The inverse design combining functionality  $f_1$  with  $f_2$  involves definition and utilization of causal factors that enable the said functionalities, and involves three steps: (1) screening materials that satisfy the enabling DPs common to the two functionalities  $f_1$  and  $f_2$ ; (2) filtering the materials according to DPs that are unique to each of the individual functionalities  $f_1$  and  $f_2$ ; and (3) by using the ensuing two compound lists of compounds  $C(f_1)$  and  $C(f_2)$  identifying the intersection between them, i.e., compounds  $C(f_1, f_2)$  possessing simultaneous  $f_1$  and  $f_2$ . Based on this process, we design 52 atomic combinations not suspected to be FERSCs that were previously synthesized. Of these 52 compounds, we find 24 FERSCs that are thermodynamically stable (i.e., reside on the convex hull) and, at the same time, feature larger spin splitting (large than 25 meV). These include BrF<sub>5</sub> (*Cmc2<sub>1</sub>*), TiIO<sub>3</sub> (*R3m*), ZnI<sub>2</sub>O<sub>6</sub> (*P2<sub>1</sub>*), LaTaO<sub>4</sub> (*Cmc2<sub>1</sub>*), Tl<sub>3</sub>S<sub>3</sub>Sb (*R3m*), Sn<sub>2</sub>P<sub>2</sub>Se<sub>6</sub> (*Pc*), and Bi<sub>2</sub>SiO<sub>5</sub> (*Cmc2<sub>1</sub>*) that have Rashba spin splitting of 31, 57, 111, 40, 90, 67, and 76 meV, respectively. Density functional theory calculations illustrate the reversal of the spin texture when the electric polarization is flipped. This paper validates a general approach for the search of other cofunctionalities based on causal enabling design principles rather than uncovering machine correlations.

DOI: [10.1103/PhysRevB.102.144106](https://doi.org/10.1103/PhysRevB.102.144106)

## I. INTRODUCTION

The traditional approach to discovering new functional materials based on combinations of guided chemical intuition with laboratory trial and error has been recently supplemented by material design based on quantum mechanics. Many compounds that have never been synthesized before have recently been predicted to be stable and synthesizable [1–8], dozens of which have actually been made and tested. This approach offers advantages over intuition-driven experimental explorations that generally involve searching for the right properties in the chemical neighborhood of known classes of materials, a process unlikely to frequently result in unexpected discoveries. Theoretically identifying materials with a given functionality  $f$  is often done via *direct approaches*: Given the identity of a compound in terms of its

atomic identities, composition, and structures (ACS), compute the property of interest for as many ACS as possible [5,6,9]. One then sifts through the results looking for a target compound with a desired functionality; the resulting target compounds will be referred to as  $C(f)$ . Successful identification of ACS with a given single functionality based on this “direct approach” includes the prediction of two-dimensional (2D) materials [10,11], topological insulators [12–14], and ferroelectric materials [15–17]. The data obtained from such direct calculations or measurements can also be used in machine learning, thereby providing an interpolation formula (in terms of phenomenological features) for the property of compounds not directly calculated via quantum mechanics [18].

Such computational searches can have their own limitations, working best for identifying a material with single target functionality but not when target *multifunctionalities* are needed. Indeed, sometimes one wishes to find materials having simultaneously more than one target functionality. Compounds with  $n$  simultaneous functionalities will be

\*carlos.mera@colorado.edu

†alex.zunger@colorado.edu

referred to as  $C(f_1, f_2, \dots, f_n)$ . Examples of known bifunctionalities ( $f_1$  and  $f_2$ ) include Rashba spin splitting (RSS) and topological insulators [19], ferroelectric ferromagnets [20,21], transparent and conducting compounds [22–24], or electrical conductors that are thermal insulators (i.e., thermoelectrics) [25,26]. The use of the above noted direct approach might become intricate for multiple target functionalities in a broad set of materials. An alternative approach is the *inverse design* that, unlike the direct approach, starts with the establishment of the target property and searches for the ACS that delivers them. Unlike machine learning that does not necessarily look for causal relations, in inverse design one establishes design principles (DPs) based on specific *causal physical mechanisms* of the relevant properties (rather than phenomenological features), followed by screening of compounds based on these physical models [27–29]. This approach can be generalized more easily to multifunctionalities by explicitly establishing the cross between the individual causal models underlying each functionality.

In the present paper we illustrate the inverse design approach based on causal physical models used as filters for seeking compounds that are simultaneously ferroelectric and Rashba semiconductors (FERSCs). This cofunctionality could provide a platform for the much sought electrical control of spin-polarized states [30]. The potential significance of this cofunctionality is based on the observations that (a) the spin texture in Rashba bands depends on the direction of the electric dipole and (b) the electric dipole and, hence, the electric polarization in ferroelectric materials can be controlled (i.e., switched) by an external electric field [31]. Consequently, a material combining both functionalities will be able to reverse the Rashba spin texture by applying external electric fields. To date, the coexistence of ferroelectricity and Rashba effects near the band edges in the same compound is extremely rare. Theoretical predictions of FERSCs focus on oxides with heavy cations, e.g.,  $\text{Bi}_2\text{WO}_6$  ( $Fmm2$ ) [32],  $\text{BiAlO}_3$  ( $P4mm$ ) [33],  $\text{SrBiO}_3$  ( $P2_1/n$ ) [34], hexagonal  $ABC$  compounds with  $\text{LiGaGe}$  structure [35,36], hybrid metal halide perovskites  $\text{CH}_3\text{NH}_3\text{PbI}_3$  ( $I4cm$ ) [37,38], two-dimensional  $\text{AgBiP}_2\text{Te}_6$  ( $P3$ ) [39], and strained  $\text{PbTiO}_3$  [40], or heavy anion chalcogenides such as  $\text{SnTe}$  ( $R3m$ ) [41–43]. However, the Rashba bands originating from heavy cation orbitals are often not positioned energetically at the valence- or conduction-band edges (because cation orbitals are not usually there) [32,44]. Furthermore, heavy anion chalcogenides such as  $\text{SnTe}$  have a relatively small experimentally measured band gap of 0.33 eV [45]. In fact,  $\text{GeTe}$  ( $R3m$ ) is the only experimentally verified three-dimensional (3D) FERSC [30,46,47] to have a large Rashba coefficient of 4.9 and 2.5 eVÅ in the valence-band maximum (VBM) and the conduction-band minimum (CBM) [19], respectively, and a (experimental) band gap of  $\approx 0.61$  eV [45]. In two-dimensional ferroelectric Dion-Jacobson perovskites, the Rashba coefficient and spin splitting have experimentally been confirmed to be 4.9 eVÅ and 85 meV, respectively [48].

Each functionality, as shown in Fig. 1, is enabled by design principles that are either identical with the DPs that enable other functionalities [“common DPs”—see the first three items enabling Rashba and ferroelectricity in Figs. 1(a) and 1(b), respectively] or unique to that functionality [unique

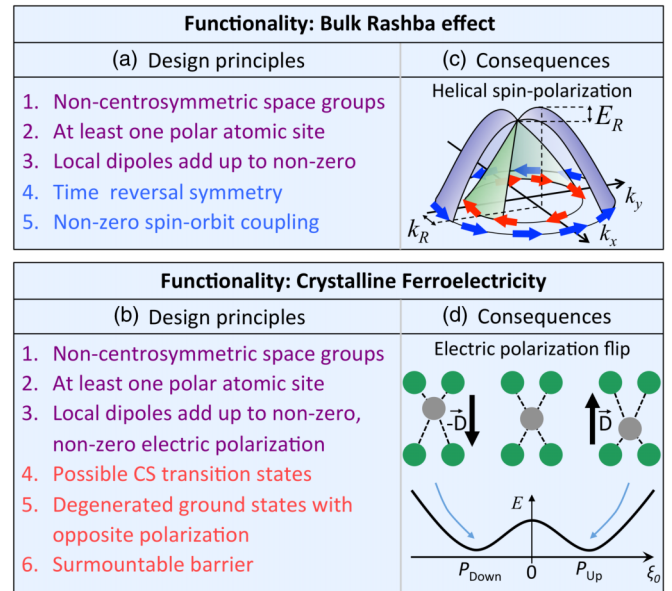


FIG. 1. Design principles (a, b) and their consequences (c, d) for the Rashba effect and for ferroelectricity. In (c), the spin texture is represented by red and blue. The Rashba spin splitting and momentum offset are represented by  $E_R$  and  $k_R$ , respectively. The bulk Rashba coefficient is given by  $\alpha_R = 2E_R/k_R$ . Common DPs are in purple and individual (unique) DPs in blue and red. In (d), the double-well electric potential is schematically represented (black line) as a function of the ferroelectric polarization. The gray atoms in (d) are forming atomic layers that are equidistant from the green atoms for zero polarization. The two degenerated ground states corresponding to opposite ferroelectric polarization directions ( $P_{\text{Down}}$  and  $P_{\text{Up}}$ ) are given by opposite atomic displacements

DPs—see items a4 and a5 for Rashba in Fig. 1(a) and items b4–b6 for ferroelectrics in Fig. 1(b)). The essential design concepts underlying the cofunctionality search are based on three steps.

(1) Screen materials from a database that satisfy the enabling DPs common with other functionalities  $f_1$  and  $f_2$ .

(2) Using the resulting list of materials that satisfy common DPs, filter the materials according to DPs that are unique to each of the *individual functionalities*  $f_1$  and  $f_2$ . This step results in two sets of compounds  $C(f_1)$  and  $C(f_2)$ .

(3) Using the two compound lists  $C(f_1)$  and  $C(f_2)$ , identify the intersection between these lists, i.e., compounds  $C(f_1, f_2)$  possessing simultaneous  $f_1$  and  $f_2$ . If the cofunctionality requires additional conditions that are not part of those enabling the single functionalities  $f_1$  and  $f_2$ , this last step would involve the filtering of compounds based on the DPs that are unique for the cofunctionality.

Figure 1(a) lists the enabling DPs for the bulk Rashba effect, whereas Fig. 1(b) lists the enabling DPs for bulk ferroelectricity. Conditions 1–3 are common to Rashba and ferroelectrics, whereas the remaining conditions in each case are unique to each functionality. This approach aims to design multifunctionalities, even if these were previously synthesized but unnoticed as possessing the required functionality.

In addition to the necessary DPs that *enable* the pertinent functionalities, there might exist other DPs responsible for

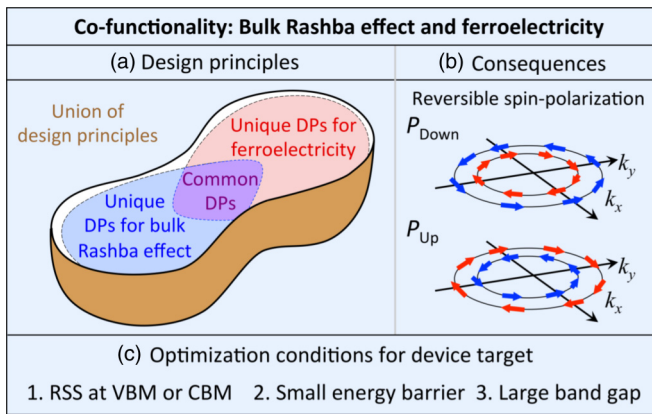


FIG. 2. Design principles and consequences of the FERSC co-functionality. (a) The enabling conditions are the union of DPs enabling the Rashba effect and ferroelectricity (the brown peanut is the union of all DPs). The color code for overlapping and unique DPs is the same as specified in Fig. 1. (b) The consequence of this co-functionality is the reversal of the spin texture by flipping the electric polarization. The spin texture is represented by red and blue, and the dipole direction is represented by the black arrow. Polarizations up and down have opposite spin textures. (c) Optimization conditions for specific device application: (c1) Rashba spin splitting (RSS) near the band edges (VBM and CBM) to access the spin-polarized states without shifting the Fermi energy, (c2) small ferroelectric energy barrier, which enhance the ferroelectric polarization switching, and (c3) large bandgap to avoid the large leakage currents observed in ferroelectric/electrode interfaces.

optimizing the functionalities for certain applications. For compounds that have both Rashba effect and are ferroelectric (FERSCs), this could include useful targets such as requiring that (i) the Rashba spin splitting should be located energetically near the band edges, rather than deep in the bands (so that these states could be accessed without shifting the Fermi energy, e.g., via doping); (ii) there should be a sufficiently large linear-in- $k$  spin splitting (e.g., more than 25 meV); and (iii) the band gap should be sufficiently large, 0.5 eV for instance (so as to prevent large leakage currents observed in electrode-ferroelectric interfaces [49,50]). These conditions for optimization of the co-functionality are given in Fig. 2(c). We do not consider here more detailed optimizations such as spin lifetime and mobilities. We will refer to these conditions (i–iii) as “optimizing DPs” needed for applications, being over and beyond the essential conditions enabling the very coexistence of ferroelectricity and Rashba effect (“enabling DPs”).

Our starting point is a database of 6355 compounds preserving time-reversal symmetry (i.e., nonmagnetic) that have nonzero band gaps and were previously synthesized. We have previously extracted these 6355 nonmagnetic insulator compounds [19] from the Automatic-Flow (AFLOW) database [5] that started from the Inorganic Crystal Structure Database (ICSD) [51], finding 20 831 unique compounds with less than 20 atoms per unit cell. As shown in Fig. 3, applying DPs common to both functionalities (step 1) leaves 867 compounds; applying next the DPs that are unique to each of the two functionalities (step 2) leaves 619 and 262 potential Rashba and ferroelectric materials, respectively. The intersection between these two lists of compounds (step 3) leads to 199 Rashba

ferroelectric cofunctional compounds. Filtering further according to the optimizing DPs of Fig. 2(c) with Rashba band restricted to be at either VBM or CBM leaves 60 cofunctional compounds with linear-in- $k$  spin splitting, of which 47 have a ferroelectric energy barrier less than 1 eV per atom. Using this approach we confirm the previously known FERSC behavior of GeTe ( $R3m$ ) [47,50]. This procedure reveals a list of 52 previously synthesized compounds that were not previously realized to be FERSCs, of which 24 FERSCs are thermodynamically stable (i.e., reside on the convex hull). In this list of stable compounds, we find FERSCs featuring giant spin splitting, i.e., as large as reported in previous works (e.g., GeTe [50] with 4.9 and 2.5 eVÅ in the VBM and CBM, respectively). For instance, BrF<sub>5</sub> ( $Cmc2_1$ ), TiO<sub>3</sub> ( $R3m$ ), ZnI<sub>2</sub>O<sub>6</sub> ( $P2_1$ ), LaTaO<sub>4</sub> ( $Cmc2_1$ ), Tl<sub>3</sub>S<sub>3</sub>Sb ( $R3m$ ), Sn<sub>2</sub>P<sub>2</sub>Se<sub>6</sub> ( $Pc$ ), and Bi<sub>2</sub>SiO<sub>5</sub> ( $Cmc2_1$ ) have large Rashba spin splitting of 31, 57, 111, 40, 90, 67, and 76 meV, respectively. In this specific group of materials, we find seven ferroelectric Rashba materials with Rashba coefficient larger than 2 eVÅ (PbS, TiO<sub>3</sub>, ZnI<sub>2</sub>O<sub>6</sub>, Tl<sub>3</sub>S<sub>3</sub>Sb, Bi<sub>2</sub>CO<sub>5</sub>, KCuBi<sub>2</sub>S<sub>4</sub>, and KIO<sub>3</sub>), which can enhance the spin-polarization reversion. The prediction of FERSC and novel spin-polarization effects can open the way for novel device applications, also establishing a standard inverse design approach for the search of other cofunctionalities. We hope that some or all predictions (Tables II–IV below) will be tested experimentally.

## II. DESIGN PRINCIPLES FOR THE TARGET FUNCTIONALITIES: RASHBA, FERROELECTRICITY, AND BOTH

We now describe how the three-steps selection is done with reference to  $f_1$  = Rashba effect and  $f_2$  = crystalline ferroelectricity.

### A. The Rashba effect: Design principles for its existence in a bulk compound

The bulk Rashba effect is defined as the spin splitting generated by the breaking of the inversion symmetry induced by an electric potential. Here, we discuss the bulk Rashba effect [52,53] and not the surface or interface one. The enabling conditions [Fig. 1(a)] for the existence of this effect in bulk materials are [54] (a1) breaking of the inversion symmetry via noncentrosymmetric (NCS) space group with (a2) at least one polar atomic site and (a3) local dipoles that add up to nonzero. In addition to DPs a1–a3 that guarantee the asymmetry of the electric potential, and are common also to ferroelectrics, Rashba compounds also need to have (a4) time-reversal symmetry (i.e., be nonmagnetic), which guarantees that the spin texture will depend only on the electric polarization direction, and (a5) the existence of spin-orbit coupling (SOC), required for guaranteeing a nonzero Rashba spin splitting.

In addition to these Rashba enabling conditions, there are some *optimization conditions needed for specific applications* but not necessary for the existence of the Rashba effect. These include RSS larger than 25 meV located energetically near band edges, and larger Rashba coefficient, which can enhance spin-current conversion. The *consequences* of the Rashba enabling conditions a1–a5 include nondegenerated spin bands

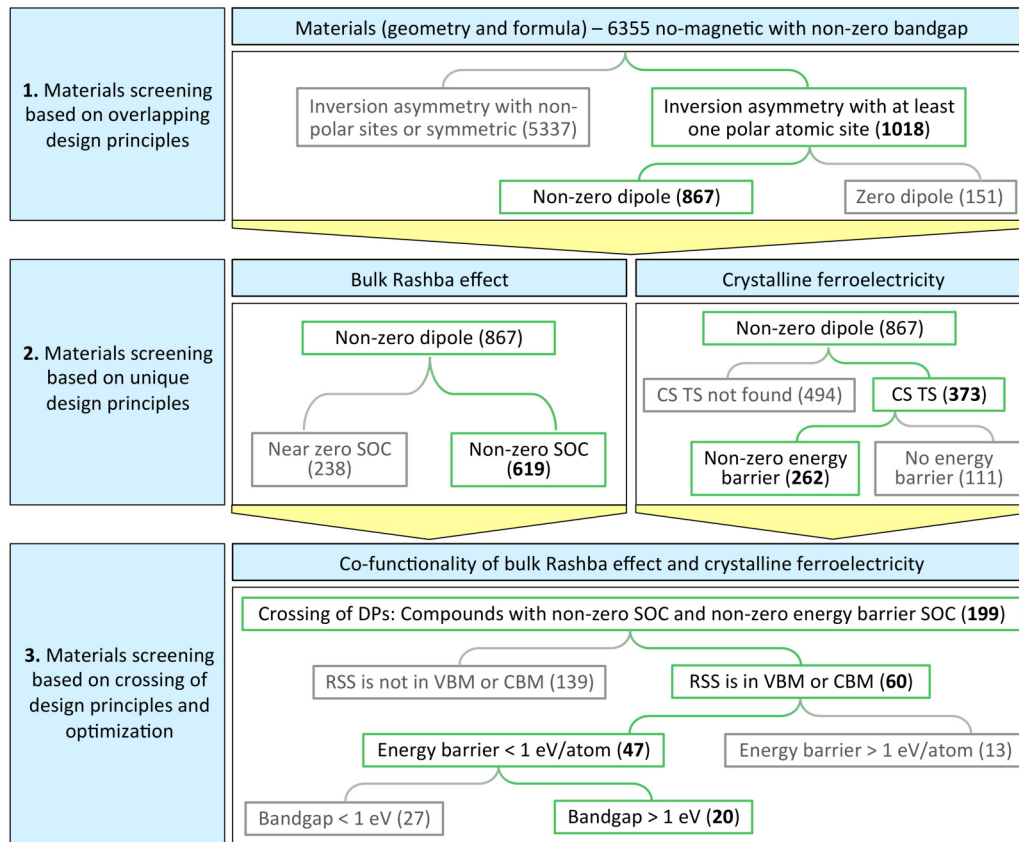


FIG. 3. Materials screening based on (line 1) the overlapping of design principles enabling single functionalities, (line 2) unique design principles for single functionalities, and (line 3) the crossing of the resulting lists. Additional design principles for the optimization of the cofunctionality for device applications are also included in step 3.

with helical spin texture perpendicular to the asymmetric potential, as represented in Fig. 1(c). The direction of this spin polarization depends on the electric dipole, i.e., opposite dipole direction leads to opposite spin-polarization direction.

#### Abundance of Rashba compounds

Only few compounds have been reported thus far to have a large bulk Rashba coefficient, which is defined as the ratio between the spin splitting  $E_R$  and the momentum offset  $k_R$ , i.e.,  $\alpha_R = 2E_R/k_R$  [Fig. 1(c)]. For this reason it has been thought that the Rashba effect is rather rare in nature [55]. Known examples include GeTe ( $R3m$ ) [30,47], BiTeI ( $P3m1$ ) [52,56], metallic PtBi<sub>2</sub> [57], the 2D organic-inorganic halide perovskite  $(C_6H_5C_2H_4NH_3)_2PbI_4$  [58], and the topological insulator PrGe ( $P3m1$ ) [59].

Based on the enabling design principles a1–a5 listed in Fig. 1(a) and starting from the AFLOW-ICSD database containing 20 831 unique compounds with less than 20 atoms per unit cell, we have recently created a list of 199 bulk Rashba compounds using density functional theory (DFT) based calculations [19]. We have further shown [19] that one can classify them to strong vs weak Rashba compounds based on whether the Rashba bands show anticrossing (corresponding to strong, i.e.,  $\alpha_R$  larger than  $\approx 1.3$  eVÅ), or if there are no anticrossing bands (corresponding to weak Rashba). This separates the 199 Rashba compounds to 165 weak and 34 strong

Rashba compounds. All were previously synthesized, but were largely not recognized to be Rashba materials [19]. The list of the predicted Rashba compounds is given in Ref. [19].

#### B. Ferroelectricity: Design principles for its existence in compounds

Ferroelectric materials can be classified as displacive or order-disorder [60]. Displacive ferroelectric compounds [61,62], which are the focus of this paper, are mainly characterized by a double-well potential [Fig. 1(d)] where the two degenerated ground states have nonzero total electric polarization [63]. The enabling conditions [see design principles in Fig. 1(b)] for the existence of the displacive ferroelectricity are (b1) noncentrosymmetric space group, (b2) the existence of at least one polar atomic site, and (b3) the presence of local dipoles that add up to nonzero. In addition to these conditions that are identical to the enabling conditions of Rashba, displacive ferroelectrics also must have additional enabling conditions: (b4) a possible centrosymmetric transition state (TS) [top of the activation barrier in Fig. 1(d)] as traditionally considered [63,64] and (b5) a degenerate ground state with two opposite polarization directions with (b6) a surmountable energy barrier (note that condition b6—a surmountable barrier—does not mean that the barrier is necessarily small). Conditions b1–b3 guarantee the nonzero ferroelectric polarization, i.e., the density of electric dipoles, whereas conditions

b4 and b5 guarantee the existence of the double well necessary in displacive ferroelectrics. In ferroelectrics, the transition state can also have multiple local motifs with nonzero local electric polarization that add up to zero (i.e., paraelectric structure) [65–67]. The theoretical modeling of this polymorphous structure requires the energy minimization with respect to the number of atoms used to define the unit cell [68,69]. Here, we restrict condition b4 to the one-unit-cell model (i.e., only one centrosymmetric local motif) as traditionally considered [54,55]. Additionally, nonzero band gap is usually also referred to as a necessary condition for displacive ferroelectricity; however, it has recently been found that metals can also have spontaneous electric polarization [70].

In addition to these enabling conditions, there are some *optimization conditions needed for specific applications* but not needed for the existence of ferroelectricity. For instance, the energy barrier is a measure of how easy it is to flip polarization, meaning that ferroelectric compounds with smaller energy barriers typically require smaller switching electric fields.

The *consequences* [Fig. 1(d)] of the enabling conditions (b1)–(b6) for the ferroelectric effect include the electric control of the electric dipole. Specifically, as represented in Fig. 1(d), the electric dipole  $D$  ( $-D$ ) can be achieved by the upward (downward) atomic displacement of a structure with zero electric polarization (condition b5). The external electric fields can then induce the necessary atomic deformations to change the direction of the local electric dipoles [black arrows in Fig. 1(d)] and, consequently, the direction of the electric polarization.

#### Abundance of ferroelectric compounds

The recent direct approach search for novel ferroelectric materials has found a rather short list of 13 oxide and two nitride compounds [16], suggesting that the conditions required for ferroelectricity might be rare in nature. Most of the few predicted crystalline ferroelectric materials have corner sharing octahedra (i.e., are perovskites) formed by transition metals and oxygen, e.g.,  $ABO_3$  where  $A$  is a transition metal. It was recently discussed why perovskites with small tolerance factors are not ferroelectric: their coordination preferences of the  $A$ -site cation stabilize the  $Pnm$  structure, which suppresses the ferroelectricity observed in  $B$ -site off-centering structures (e.g.,  $BaTiO_3$  and  $PbTiO_3$ ) [71].

#### C. Design principles for coexistence of Rashba and ferroelectricity in compounds

In Fig. 2 we illustrate the common design principle for the individual functionalities, the unique conditions specific to the individual functionalities, and the union of DPs represented in a “peanut” scheme that illustrates the proposed strategy for the identification of DPs for cofunctionalities. For FERSCs, the union of the two groups of design principles for the Rashba effect [Fig. 1(a)] and for ferroelectricity [Fig. 1(b)] leads to the design principles for their cofunctionality, i.e., conditions a1–a5 plus b1–b6. The common conditions are a1–a3, identical to b1–b3. The remaining unique conditions are time-reversal symmetry (a4), nonzero SOC (a5), barrier structure with zero polarization (b4), degenerate ground state with

opposite polarization (b5), and surmountable barrier (b6). An interesting consequence of the enabling conditions for FERSC is that different polarization states have opposite helical spin polarization. This allows the reversion of the spin texture by flipping the electric polarization. This mechanism has been experimentally verified [72].

In addition to these FERSC enabling conditions, there are also optimization conditions needed for applications, e.g., in spintronic devices, but they are not necessary for the existence of FERSC. These are listed in Fig. 2(c): Rashba spin splitting near the band edges (VBM and CBM) (c1), large band gap (i.e., larger than 1eV) (c2), and small ferroelectric energy barrier (c3). A compound with these conditions allows for the efficient reversal of the spin polarization by means of external electric fields, as represented in Fig. 1(e). This is of special interest for spintronic devices such as the spintronic transistor [73].

#### Abundance of FERSC

There is no study to our knowledge that attempts to enumerate or illustrate FERSCs. GeTe (space group  $R3m$ ) is the only fabricated FERSC with large Rashba coefficients at band edges, but it has a small theoretical band gap of  $\approx 0.3$  eV. The natural arena for looking for FERSCs would be oxide perovskites; however, the Rashba spin splitting at the band edges is almost negligible (less than 1 meV) [32,40] because the VBM is formed by the low SOC oxygen  $p$  orbital and the CBM is composed of transition-metal  $d$  orbitals that are perpendicular to the electric dipole.

### III. METHODOLOGY FOR APPLYING THE DESIGN PRINCIPLES TO SEARCH FOR COMPOUNDS THAT ARE RASHBA, FERROELECTRIC, OR BOTH (FERSC)

Figure 2 indicates that for a general material to be both Rashba and ferroelectric one needs the following: the compound is noncentrosymmetric (a1, b1) with at least one atomic polar site (a2, b2) and with local dipoles that add up to nonzero (a3, b3), has time-reversal symmetry (a4), has nonzero SOC (a5), has a degenerate ground state with opposite polarization (b4), has a surmountable barrier (b5), and has a barrier structure with zero polarization (b6). In this section, we explain the materials screening process of FERSCs based on the proposed strategy for the identification of DPs of cofunctionalities, namely, (1) filtering based on overlapping DPs, (2) filtering based on mutually exclusive DPs, and (3) filtering based on crossing DPs. These proposed steps for the screening of compounds  $C(f_1, f_2)$  are illustrated in Fig. 3.

#### A. Methodology for step 1: Screen materials that satisfy the enabling DPs common with other functionalities $f_1$ and $f_2$

Our starting point is a database of 6355 compounds preserving time-reversal symmetry (i.e., nonmagnetic) that have nonzero band gap (listed in the ICSD [51]), as described in line 1 of Fig. 3. These 6355 nonmagnetic insulator compounds were previously obtained by us [19] from the initial AFLOW-ICSD database containing 20 831 unique compounds with less than 20 atoms per unit cell [5]. In our previous work, we selected compounds preserving the time-reversal symmetry

(i.e., nonmagnetic), which results in 13 838 compounds, from which 6355 are gapped and nonmagnetic (i.e., band gap larger than 1 meV). As noted above [Fig. 2(a)], step 1 is the filtering based on the common design principles (i.e., a1–a3 and b1–b3 in Fig. 1) of this initial list of 6355 nonmagnetic insulator compounds.

Following the scheme from Fig. 3 we then have the following steps.

(1) Find the subset of nonmagnetic gapped compounds that has noncentrosymmetric space group with at least one polar atomic site (filters a1 and b1 and filters a2 and b2 in Fig. 1). We use the space group of the compounds to filter materials with NCS polar atomic sites (i.e., polar space groups). The list of point groups with at least one polar site is given in Table I. This gives 1018 NCS compounds with at least one polar atomic site and another list of 5337 compounds with either CS or NCS nonpolar space group, as represented in line 1 of Fig. 3.

(2) Find the subset of NCS polar compounds that has nonzero electric dipole (filters a3 and b3 in Fig. 1): The cancellation of dipoles can be geometrically determined for each atomic site by considering vectors along the atomic bonds. Specifically, the electron transfer given by the atomic bonding of two different elements creates a microscopic dipole which direction is opposite to electron transfer direction. For a given atomic site, if all neighbor atoms were locally distributed in such a way that the dipole vectors generated by each bonding cancel each other, then the local atomic site dipole would be zero, e.g., nonpolar atomic sites. This gives an intuitive way to verify the local cancellation of dipoles using only the atomic positions and lattice vectors. Nonzero local dipoles can only be found in polar atomic sites. However, local dipoles can add up to zero for first or second neighbors or be near zero dipole for more distant atomic neighbors (e.g., atomic distances larger than the sum of van der Waals radius for two given elements), which can also be verified geometrically. From the 1018 NCS nonmagnetic insulator with at least one polar site, we identify 867 compounds with nonzero dipole and 151 compounds in which local dipoles cancel each other. The proposed approach based on the geometrical information can result in false positives nonzero dipole, since the electron dipole also depends on the specific chemical species, which requires more exhaustive first-principles calculation. We retain the 867 compounds with nonzero electric dipole for our next step.

## B. Methodology for step 2: Filter the materials according to DPs that are unique to reach the individual functionalities $f_1$ and $f_2$

The second step of the searching process is the filtering based on unique design principles (line 2 in Fig. 3). These are enabling design principles for the single functionalities that are not in the overlapping region shown in the peanut scheme of Fig. 2. For FERSCs, the “unique” DPs enabling the Rashba effect are a4 and a5 [see Fig. 1(a)], whereas the ones enabling ferroelectricity are b4, b5, and b6 [see Fig. 1(b)]. This screening process leads to two individual lists of compounds  $C(f_1)$  and  $C(f_2)$  having only one functionality ( $f_1$  or  $f_2$ ).

### 1. Constructing a list of Rashba materials from DPs validated by DFT

For a material that already has nonzero polarization to be ferroelectric, one needs to fulfil only two (additional) conditions: (a4) time-reversal symmetry and (a5) nonzero spin-orbit coupling. We apply these two filters to the list of 867 NCS polar nonmagnetic insulators with nonzero dipole obtained from step 1. As noted above, this initial list of compounds is nonmagnetic, meaning the compounds selected in step 1 intrinsically satisfy condition a4. Thus, condition a5 is the only one (additional) required to filter out materials that are potentially Rashba. For future works, it is important to note that, in the database we used as a starting point, some false positive nonmagnetic compounds could have been selected [19], since AFLOW-ICSD [5] decided if a structure is magnetic based on a limited range of trial magnetic configurations. The complete characterization of the magnetic state requires more expensive calculations.

a. Find the subset of NCS nonmagnetic insulators with nonzero dipole that have nonzero SOC [filter a5 in Fig. 1(a).] The spin-orbit coupling induces an effective magnetic field that preserves the time-reversal symmetry. In the phenomenological model describing the Rashba effect, the Rashba spin splitting  $E_R$  is proportional to the strength of the atomic SOC  $\lambda_{\text{SOC}}$  [19,55,74], i.e.,  $E_R = a\alpha_R k_R$  with  $\alpha_R = 2\lambda_{\text{SOC}}$ ,  $a$ , and  $k_R$  being the Rashba coefficient, lattice constant, and momentum offset, respectively. Almost negligible atomic SOC can be found in elements with atomic number smaller than 30 [75]. The selection of compounds formed by at least one element with atomic number larger than 30 leads to 619 compounds with nonzero SOC and 238 with almost zero SOC (Fig. 3, line 2—Rashba effect panel). We retain the 619 compounds with nonzero SOC for our next step. The spin splitting of selected Rashba compounds is not necessarily linear in  $k$ , since we did not consider this restriction in the filtering process. Thus, compounds in this list can have not only linear-in- $k$  spin splitting [19], but also cubic [76] or high-order-in- $k$  Rashba terms [77].

### 2. Constructing a list of ferroelectric materials from DPs validated by DFT

For a material that already has nonzero polarization, to be a ferroelectric one needs to fulfil only three (additional) conditions: (b6) the existence of a surmountable barrier, (b5) the existence of a degenerated ground state with two opposite polarization directions (one for each part of the double well), and (b6) the existence of a centrosymmetric configuration with zero electric polarization. We then apply the three filters to the list of 867 NCS polar nonmagnetic insulators with nonzero dipole obtained from step 1. This initial list of compounds intrinsically has nonzero band gap, a condition usually stated as necessary for ferroelectricity. Since ferroelectric metals have recently been proposed, nonzero band gap is not included as a design principle enabling ferroelectricity [Fig. 1(b)].

The existence of two polarization states on either side of the double well connected by atomic displacements requires that the material can be adiabatically deformed into at least one transition state configuration with a higher symmetry space group [DP b4 in Fig. 1(b)]. These high-symmetry

structures are traditionally assumed to have zero electric polarization, meaning that their space groups are CS. If the spontaneously electrically polarized structure has lower internal energy than the CS transition state, then an energy barrier separating opposite polarization states exists [DP b5 in Fig. 1(b)]. This barrier has to be surmountable to allow ferroelectric properties [DP b6 in Fig. 1(b)].

*a. Identify from compounds with nonzero polarization those that can be deformed into the CS transition state [filter b4 in Fig. 1(b)].* Among the list of 230 crystalline space groups, as given by Table I, the CS ones have space-group numbers (arranged into a 3D Bravais lattice): triclinic (1), monoclinic (10–15), orthorhombic (47–74), tetragonal (83–88 and 123–142), rhombohedral (147, 148, and 162–167), hexagonal (175, 176, and 191–194), and cubic (200–206 and 221–230). For each nonpolar nonmagnetic insulator obtained from step 1, we determine all the symmetry groups that can be generated only by atomic displacements (from the original atomic positions) and classify them into the classes defined as centrosymmetric space groups (see Table I). The symmetry group identification in the displacive structures is performed using the symmetry detection algorithm of pymatgen [78] using atomic displacements with steps of 0.1 Å from 0 to 2.0 Å. This procedure classifies the initial group of 867 compounds into 373 materials with CS transition state structures and 494 compounds without any high-symmetry CS transition state structures that could be obtained by deforming the initial structure. We retain the 373 materials with CS transition state structures for the next filtering process (lines 2 in Fig. 3—ferroelectric panel).

*b. Find the subset of compounds with CS transition state in which the electric polarized structure has lower total energy than the transition state [DP b5 in Fig. 1(b)].* The ferroelectric structure has to be the ground state to guarantee that the compound is spontaneously electrically polarized. In other words, the CS transition state is not more stable. This condition implies that the energy barrier (the difference in total energy of the transition state structure and the structure with electric polarization) is not zero. In order to examine this, we perform high-throughput density functional theory calculations mapping the double well for all 373 previously selected compounds with centrosymmetric transition state configuration. The DFT calculations of the double well are performed without spin-orbit coupling using Perdew-Burke-Ernzerhof (PBE) generalized gradient approximation [79] as the exchange-correlation functional and the Coulomb self-repulsion on-site term  $U$  for transition metals [80] as implemented in the Vienna Ab-Initio Simulation Package [81,82]. All the specific settings of the calculations (e.g., cutoff energies,  $k$ -point sampling, and effective  $U$  parameters) were the same as those used on the AFLOW database [5]. Based on our calculation, we find 262 compounds out of 373 having a CS transition state with positive barrier and thus they satisfy the conditions of being ferroelectrics (lines 2 in Fig. 3—ferroelectric panel). We retain these 262 potential ferroelectric materials for the next step.

*c. Subset of potential ferroelectric compounds that have a surmountable potential-energy barrier [DP b6 in Fig. 1(b)].* The energy barrier connecting the two polarization states must be lower than the dielectric strength, which counts for the *switchability* of the polarization under an external

electric field. The DFT-calculated energy barriers can only be used as a qualitative measure indicating the possibility of polarization flip. In a more realistic scenario, the electric polarization flip involves other effects, e.g., ferroelectric domains, impurities, the electric response of the substrate, and attempt frequencies. Here, we find that 196 potential ferroelectric compounds have energy barriers smaller than 1 eV/atom. Due to the used theoretical approximation (e.g., the PBE exchange-correlation functional), the filtering process based on the energy barrier could exclude many possible ferroelectric compounds. We then analyze the behavior of the energy barrier as a condition for device applications (see next section). Thus, the last step of the materials screening of compounds having the cofunctionalities of Rashba effect and ferroelectricity involves all 262 potential ferroelectric materials predicted to have nonzero energy barrier.

### C. Methodology for step 3: Identify compounds possessing simultaneous $f_1$ and $f_2$

The third step for the identification of compounds that possess a given cofunctionality consists of the union of the DPs enabling the individual functionalities. The crossing of DPs is represented in Fig. 2(a) as a peanut diagram. In practice, the overlapping region of the lists of compounds with single functionalities corresponds to bifunctional compounds. For the specific case of FERSCs, we compare our databases of Rashba and ferroelectric materials constructed in step 2. This process leads to 199 potential cofunctional compounds, 420 compounds that are only Rashba materials (i.e., these do not have centrosymmetric transition states), and 63 compounds that are only ferroelectric materials (i.e., these have near-zero SOC). We retain these 199 potential ferroelectric Rashba semiconductors for the next filtering process based on the DPs for the optimization of the cofunctionality intended to satisfy conditions for possible spintronic applications: (i) linear-in- $k$  Rashba spin splitting near the VBM and CBM band edges (so that these states could be accessed without shifting the Fermi energy, e.g., via doping)—DP for optimization c1 in Fig. 2(c); (ii) small enough energy barrier to allow electric polarization flip with relatively smaller electric fields—DP for optimization c2 in Fig. 2(c); and (iii) not too small band gap, say, 1 eV (which may have prevented switching of the ferroelectric polarization due to the large leakage currents observed in electrode-ferroelectric interfaces [49])—DP for optimization c3 in Fig. 2(c).

#### 1. Sort out the subsets of FERSCs that have Rashba spin splitting at the VBM or CBM [optimization DPs c1 in Fig. 2(c)]

We evaluate the energy position of the Rashba spin splitting in the band structure. For this purpose, we perform high-throughput DFT calculations (using the computational setup discussed in the previous section) of the orbital-resolved band structure and spin texture including SOC for the 199 FERSC candidates obtained from the crossing of DPs. We then restrict the materials screening to compounds with RSS at the VBM (CBM) or less than 30 meV below (above) the VBM (CBM). Applications also require a measurable splitting; we then select compounds with RSS larger than 1 meV. According to our calculation, this filter separates the 199 FERSC

TABLE I. Space-group indices for 3D Bravais lattices classified according to the inversion symmetry as centrosymmetric, NCS nonpolar, and NCS polar.

	Space groups for the 3D Bravais lattices						
	Triclinic	Monoclinic	Orthorhombic	Tetragonal	Rhomb.	Hexagonal	Cubic
NCS polar	1	3–9	25–46	99–110 75–82	156–161 143–146	183–186 168–173	
NCS nonpolar			16–24	89–98 111–122	149–155	174, 177–182 187–190	195–199 207–220
Centrosymmetric	2	10–15	47–74	83–88 123–142	147–148 162–167	175–176 191–194	200–206 221–230

candidates in 60 compounds with RSS at the VBM or CMB larger than 1 meV, and 139 compounds with RSS smaller than 1 meV or far from the VBM or CBM or nonlinear-in- $k$  spin splitting. After this inverse design optimization process, we retain the 60 FERSC candidates with RSS larger than 1 meV at the VBM or CMB for the next filter. Excluding the very well-known FERSC GeTe ( $R3m$ ) and seven duplicated entries with different ICSD identifier (i.e., the same compound obtained from different synthesis processes), the inverse design and optimization process leads to 52 novel ferroelectric Rashba candidates with Rashba bands at the band edges.

**2. Sort out the subsets of FERSCs with RSS at band edges that have a not too large energy barrier [optimization DPs c2 in Fig. 2(c)]**

The electric polarization flip by external electric polarization depends not only on the magnitude of the energy barrier, but can also depend on the ferroelectric domains, impurities, and magnitude of both polar displacement and polarization. Thus, small energy barrier is not necessarily sufficient for the electric polarization to be easily surmountable. In order to give a qualitative trend in the predicted FERSC, we select compounds with energy barrier smaller than 1 eV/atom. According to our DFT calculations, in the list of 60 FERSCs, there are 47 compounds with energy barrier smaller than 1 eV/atom and 13 compounds with energy barrier larger than 1 eV/atom.

**3. Sort out the subsets of FERSCs with RSS at band edges and small energy barrier that have a not too small band gap [optimization DPs c3 in Fig. 2(c)]**

For applications, a sufficiently small band gap is necessary to allow Fermi level control. In contrast, a sufficiently large band gap is necessary to allow electric polarization flip. FERSCs usually have small bandgaps (say 0.3 eV). We have selected 27 predicted FERSCs that have band gap smaller than 1 eV and 20 that have band gap larger than 1 eV. This classification is based on the direct inspection of the DFT band-structure calculations including SOC.

The results of the materials screening based on the proposed three-step strategy are summarized in Tables II–IV. Specifically, experimentally synthesized compounds at the convex hull (i.e., energy above the convex hull equal to zero,  $E_{\text{ch}} = 0$  meV) are in Table I, experimentally synthesized compounds with energy above the convex hull (i.e.,  $E_{\text{ch}} > 0$  meV) are in Table II, and compounds for which the experimental

details are missing are in Table III (i.e., potential FERSCs with hypothetical structure with and without  $E_{\text{ch}} = 0$  meV).

#### IV. DISCUSSION OF THE PREDICTED FERROELECTRIC RASHBA MATERIALS

The list of compounds identified as FERSC includes known ferroelectrics such as GeTe and also 52 previously synthesized compounds that were previously not noted to be Rashba materials, e.g., PbS in the  $Pma2$  structure and BrF<sub>5</sub> in the  $Cmc21$  structure. These are classified in terms of the energy above the convex hull: 24 FERSCs at the convex hull (Table II) and 18 FERSCs with energy above the convex hull greater than zero (Table III). Eleven compounds that are hypothetical or fabricated with missing information are shown in Table IV. We identify seven duplicated entries, which are not presented in Tables I–IV. These and their ICSD identifiers are Rb<sub>4</sub>CO<sub>4</sub> (245 436), NbLiO<sub>3</sub> (28 299, 94 493), GeTe (659 808, 659 811, 56 040), and PbS (183 249). These duplicated entries have similar space groups and the same composition of the compounds listed in Tables II–IV, but higher  $R$  factor. The proposed inverted design of cofunctionalities reveals then 52 novel ferroelectric Rashba candidates with Rashba bands at the band edges. In this section, we discuss the electric properties and spin polarization of these predicted ferroelectric Rashba compounds.

##### A. Trends in predicted FERSCs

In the list of predicted FERSCs, we find compounds featuring giant spin splitting, i.e., as large as in GeTe (160 meV) [50]. Other compounds such as BrF<sub>5</sub> ( $Cmc21$ ), TiIO<sub>3</sub> ( $R3m$ ), ZnI<sub>2</sub>O<sub>6</sub> ( $P2_1$ ), LaTaO<sub>4</sub> ( $Cmc2_1$ ), Ti<sub>3</sub>S<sub>3</sub>Sb ( $R3m$ ), Sn<sub>2</sub>P<sub>2</sub>Se<sub>6</sub> ( $Pc$ ), and Bi<sub>2</sub>SiO<sub>5</sub> ( $Cmc2_1$ ) have large Rashba spin splitting of 31, 57, 111, 40, 90, 67, and 76 meV, respectively. In this specific group of materials, we find seven ferroelectric Rashba materials with Rashba coefficient larger than 2 eVÅ (PbS, TiIO<sub>3</sub>, ZnI<sub>2</sub>O<sub>6</sub>, Ti<sub>3</sub>S<sub>3</sub>Sb, Bi<sub>2</sub>CO<sub>5</sub>, KCuBi<sub>2</sub>S<sub>4</sub>, and KIO<sub>3</sub>). However, we also find smaller RSS and ferroelectrics with weak Rashba effect (see Tables II–IV). Additionally, we provide the difference between the DFT internal energy of the transition state structure with zero polarization and the structure with electric polarization (ferroelectric barrier). This theoretical value can be used as a qualitative measure indicating the possibility of polarization flip. As a matter of fact, in Table II, we only consider compounds with barriers smaller than 1 eV/f.u. In practice, the electric polarization flip



TABLE II. Previously fabricated ferroelectric Rashba candidates on the convex hull. For each compound we present the ICSD code, energy above the convex hull ( $E_{\text{ch}}$ ) given by the materials project (meV/fu), polar space group (PSG) of the ferroelectric structure, centrosymmetric space group (CS-SG) of the transition state, difference in total energy between ferroelectric structure and transition state configuration (barrier) in meV, Rashba spin splitting (RSS) in meV, momentum offset ( $k_R$ ) in  $\text{\AA}^{-1}$ , Rashba parameters ( $\alpha_R$ ) in  $\text{eV}\text{\AA}$ , and  $R$  factor for refinement of the experimental structure. Compounds with  $E_{\text{ch}} = 0$  are on the convex hull.

Comp	ICSD	$E_{\text{ch}}$	NCS-P SG	CS-SG	Barrier	RSS	$K_R$	$\alpha_R$	$R$	Ref.
GeTe	188458	0	160 ( $R3m$ )	166 ( $R\bar{3}m$ )	19	142	0.068	4.219	0.049	[83]
Tl <sub>3</sub> S <sub>3</sub> Sb	603664	0	160 ( $R3m$ )	166 ( $R\bar{3}m$ )	801	90	0.083	2.169	0.020	[84]
Sn <sub>2</sub> P <sub>2</sub> Se <sub>6</sub>	403097	0	7 ( $Pc$ )	14 ( $P2_1/c$ )	15	67	0.163	0.820	0.049	[85]
TiIO <sub>3</sub>	62106	0	160 ( $R3m$ )	166 ( $R\bar{3}m$ )	476	57	0.052	2.184	0.025	[86]
KCuBi <sub>2</sub> S <sub>4</sub>	91297	0	36 ( $Cmc2_1$ )	63 ( $Cmcm$ )	542	51	0.035	2.947	0.017	[87]
BrF <sub>5</sub>	31690	0	36 ( $Cmc2_1$ )	63 ( $Cmcm$ )	98	31	0.127	0.484	0.184	[88]
PtF <sub>4</sub>	71579	0	43 ( $Fdd2$ )	70 ( $Fddd$ )	223	31	0.204	0.322	0.042	[89]
CsGeI <sub>3</sub>	62559	0	160 ( $R3m$ )	166 ( $R\bar{3}m$ )	17	27	0.027	1.946	0.043	[90]
Cs <sub>2</sub> Se <sub>3</sub>	14095	0	36 ( $Cmc2_1$ )	63 ( $Cmcm$ )	349	25	0.109	0.460	0.086	[91]
LiNbO <sub>3</sub>	28301	0	146 ( $R3$ )	166 ( $R\bar{3}m$ )	308	22	0.208	0.212	0.042	[92]
BaHgS <sub>2</sub>	32648	0	26 ( $Pmc2_1$ )	55 ( $Pbam$ )	145	19	0.094	0.414	0.088	[93]
Tl <sub>3</sub> AsSe <sub>3</sub>	15148	0	160 ( $R3m$ )	166 ( $R\bar{3}m$ )	410	12	0.047	0.530	0.105	[94]
Cs <sub>2</sub> Te <sub>3</sub>	53245	0	36 ( $Cmc2_1$ )	64 ( $Cmce$ )	570	10	0.063	0.303	0.118	[95]
AsF <sub>3</sub>	35132	0	33 ( $Pna2_1$ )	59 ( $Pmmm$ )	460	6	0.029	0.422	0.055	[96]
Ag <sub>2</sub> S <sub>3</sub> Te	85135	0	9 ( $Cc$ )	15 ( $C2/c$ )	285	6	0.023	0.562	0.044	[97]
Ag <sub>2</sub> HgSI <sub>2</sub>	413300	0	36 ( $Cmc2_1$ )	63 ( $Cmcm$ )	99	6	0.034	0.345	0.057	[98]
BaAs <sub>2</sub>	414139	0	7 ( $Pc$ )	14 ( $P2_1/c$ )	45	6	0.037	0.307	0.082	[99]
CsPbF <sub>3</sub>	93438	0	161 ( $R3c$ )	166 ( $R3m$ )	58	3	0.074	0.323	0.020	[100]
KLaSiSe <sub>4</sub>	603185	0	4 ( $P2_1$ )	11 ( $P2_1/m$ )	35	2	0.030	0.151	0.041	[101]
BaZnF <sub>4</sub>	402926	0	36 ( $Cmc2_1$ )	63 ( $Cmcm$ )	153	2	0.014	0.227	0.025	[102]
KTbGeS <sub>4</sub>	409811	0	4 ( $P2_1$ )	11 ( $P2_1/m$ )	47	1	0.031	0.075	0.037	[103]
SeF <sub>2</sub> O	12110	0	29 ( $Pca2_1$ )	57 ( $Pbcm$ )	5465	6	0.028	0.427	0.082	[104]
Tb <sub>3</sub> GaO <sub>6</sub>	99494	0	36 ( $Cmc2_1$ )	63 ( $Cmcm$ )	1078	1	0.043	0.055	0.035	[105]
SrCl <sub>2</sub> O <sub>6</sub>	61157	0	43 ( $Fdd2$ )	70 ( $Fddd$ )	1046	1	0.038	0.054	0.034	[106]

TABLE III. Previously fabricated ferroelectric Rashba candidates with energy above the convex hull larger than zero. For each compound we present the ICSD code, energy above the convex hull ( $E_{\text{ch}}$ ) given by the materials project (meV/fu), polar space group (PSG) of the ferroelectric structure, centrosymmetric space group (CS-SG) of the transition state, difference in total energy between ferroelectric structure and transition state configuration (barrier) in meV, Rashba spin splitting (RSS) in meV, momentum offset ( $k_R$ ) in  $\text{\AA}^{-1}$ , Rashba parameters ( $\alpha_R$ ) in  $\text{eV}\text{\AA}$ , and  $R$  factor for refinement of the experimental structure. Compounds with  $E_{\text{ch}} = 0$  are on the convex hull.

Comp	ICSD	$E_{\text{ch}}$	NCS-P SG	CS-SG	Barrier	RSS	$K_R$	$\alpha_R$	$R$	Ref.
Bi <sub>2</sub> SiO <sub>5</sub>	30995	12	36 ( $Cmc2_1$ )	63 ( $Cmcm$ )	9	76	0.157	0.969	0.052	[107]
CUO <sub>5</sub>	87760	6	44 ( $Imm2$ )	71 ( $Immm$ )	79	70	0.240	0.584	0.022	[108]
LaTaO <sub>4</sub>	97688	9	36 ( $Cmc2_1$ )	63 ( $Cmcm$ )	711	40	0.168	0.476	0.046	
BiAlO <sub>3</sub>	171708	53	161 ( $R3c$ )	166 ( $R\bar{3}m$ )	167	31	0.168	0.365	0.006	[109]
Ag <sub>5</sub> S <sub>4</sub> Sb	16987	14	36 ( $Cmc2_1$ )	63 ( $Cmcm$ )	133	13	0.063	0.408	0.097	[110]
Ta <sub>2</sub> O <sub>5</sub>	280397	91	5 ( $C2$ )	12 ( $C2/m$ )	61	7	0.028	0.530	0.026	[111]
Tl <sub>3</sub> AsS <sub>3</sub>	100292	10	160 ( $R3m$ )	166 ( $R\bar{3}m$ )	521	7	0.020	0.699	0.058	[112]
BaMgF <sub>4</sub>	50227	4	36 ( $Cmc2_1$ )	63 ( $Cmcm$ )	467	3	0.027	0.203	0.015	[113]
KIO <sub>3</sub>	97995	5	160 ( $R3m$ )	166 ( $R\bar{3}m$ )	408	2	0.002	1.993	0.017	[114]
Pb <sub>2</sub> P <sub>3</sub> HO <sub>10</sub>	2494		1 ( $PI$ )	2 ( $P\bar{1}$ )	62	1.2	0.494	0.047	0.15	[115]
Bi <sub>2</sub> CO <sub>5</sub>	94740	116	44 ( $Imm2$ )	71 ( $Immm$ )	1278	142	0.088	3.232	0.021	[116]
BiCl <sub>3</sub>	41179		31 ( $Pmn2_1$ )	63 ( $Cmcm$ )	1078	112	0.311	0.720	0.040	[117]
LiIO <sub>3</sub>	41199	4	33 ( $Pna2_1$ )	63 ( $Cmcm$ )	1712	44	0.144	0.615	0.109	[118]
AsTl <sub>3</sub> O <sub>4</sub>	407561		4 ( $P2_1$ )	63 ( $Cmcm$ )	1880	7	0.083	0.174	0.044	[119]
CdRbN <sub>3</sub> O <sub>6</sub>	95537	39	146 ( $R3$ )	166 ( $R\bar{3}m$ )	1739	2	0.025	0.115	0.059	[120]
Dy <sub>3</sub> GaO <sub>6</sub>	99495	1	36 ( $Cmc2_1$ )	63 ( $Cmcm$ )	1440	1	0.058	0.045	0.032	[105]
KCdN <sub>3</sub> O <sub>6</sub>	95538	56	146 ( $R3$ )	166 ( $R\bar{3}m$ )	1676	1	0.025	0.080	0.070	[120]
CdTlN <sub>3</sub> O <sub>6</sub>	95539	46	146 ( $R3$ )	166 ( $R\bar{3}m$ )	2227	1.1	0.025	0.088	0.079	[120]

TABLE IV. Theoretical ferroelectric Rashba candidates. For each compound we present the ICSD code, energy above the convex hull ( $E_{\text{ch}}$ ) given by materials project (meV/fu), polar space group (PSG) of the ferroelectric structure, centrosymmetric space group (CS-SG) of the transition state, difference in total energy between ferroelectric structure and transition state configuration (barrier) in meV, Rashba spin splitting (RSS) in meV, momentum offset ( $k_R$ ) in  $\text{\AA}^{-1}$ , Rashba parameters ( $\alpha_R$ ) in eV $\text{\AA}$ , and  $R$  factor for refinement of the experimental structure, where  $T$  stands for theoretical structures. Compounds with  $E_{\text{ch}} = 0$  are on the convex hull.

Comp	ICSD	$E_{\text{ch}}$	NCS-P SG	CSG	Barrier	RSS	$K_R$	$\alpha_R$	$R$	Ref.
ZnI <sub>2</sub> O <sub>6</sub>	54086	0	4 ( $P2_1$ )	14 ( $P2_1/c$ )	632	111	0.091	2.448		[121]
IrSbS	74630	4	29 ( $Pca2_1$ )	69 ( $Fmmm$ )	6489	59	0.093	1.270		[122]
BeLiSb	616318	39	186 ( $P6_3mc$ )	194 ( $P6_3/mmc$ )	3	5	0.022	0.453		[123]
CRb <sub>4</sub> O <sub>4</sub>	245438	223	8 ( $Cm$ )	12 ( $C2/m$ )	4047	5	0.078	0.117		[124]
TlBrO <sub>3</sub>	76966	8	160 ( $R3m$ )	166 ( $R\bar{3}m$ )	801	3	0.013	0.486		
Tl <sub>3</sub> AsS <sub>3</sub>	611332	10	160 ( $R3m$ )	166 ( $R\bar{3}m$ )	686	2	0.016	0.250		
PbS	183250	170	28 ( $Pma2$ )	51 ( $Pmma$ )	207	41	0.034	2.372	T	[125]
TiZnBi <sub>2</sub> O <sub>6</sub>	186801	63	99 ( $P4mm$ )	123 ( $P4/mmm$ )	247	17	0.030	1.243	T	[126]
Bi <sub>2</sub> TiZnO <sub>6</sub>	162767	63	99 ( $P4mm$ )	123 ( $P4/mmm$ )	247	11	0.022	1.022	T	[127]
PbS	183255	56	186 ( $P6_3mc$ )	194 ( $P6_3/mmc$ )	14	10	0.013	1.511	T	[125]
Ag <sub>2</sub> S	98454	0	4 ( $P2_1$ )	11 ( $P2_1/m$ )	14	1	0.042	0.066	T	[128]

involves other effects, e.g., ferroelectric domains, impurities, the electric response of the substrate, and attempted frequencies. For all fabricated compounds, we provide the  $R$  factors taken from previous works on the synthesis of these compounds.

## B. Illustration of band structure and Rashba effect along the double-well ferroelectric surface

In order to illustrate the prototypical behavior of these compounds, we show the double-well potential, band structure, Rashba spin splitting, and spin texture for the FERSC BrF<sub>5</sub> ( $Cmc2_1$ ). Figure 4 shows the double-well electric polarized structures and band structures for different electric polarizations of the FERSC BrF<sub>5</sub>.

### 1. Spontaneously polarized structure

The minimum-energy ground-state structure has  $Cmc2_1$  symmetry (on the convex hull) with a unit cell formed by 12 atoms: two bromine and ten fluorine atoms. Each Br atom (represented in gray in Fig. 4) has four F atoms as nearest neighbors (represented in blue in Fig. 4) with an interatomic distance of 1.82  $\text{\AA}$ . The second-nearest neighbor of Br atoms is one F atom (represented in cyan in Fig. 4) along the Br-Br bond. The atomic displacement with respect to a centrosymmetric structure (the transition state) creates microscopic atomic dipoles along the atomic bonds that add up to nonzero. Specifically, in BrF<sub>5</sub>, the displacement of F atoms along the vector connecting Br atoms leads to two opposite polarization directions (denoted here as polarization up and polarization down), as represented in Fig. 4. These two ground-state structures can be intertransformed by atomic position deformations, i.e., the upward or downward F-atom displacement. This creates the expected double-well behavior characterizing displacive ferroelectric materials. As presented in Fig. 4, for BrF<sub>5</sub>, the RSS increases as the electric

polarization increases, i.e., even for small atomic displacements a small electric polarization is induced, which leads to a nonzero RSS at the CBM (orange point in Fig. 4). The ground states have two polarization directions, which have Rashba

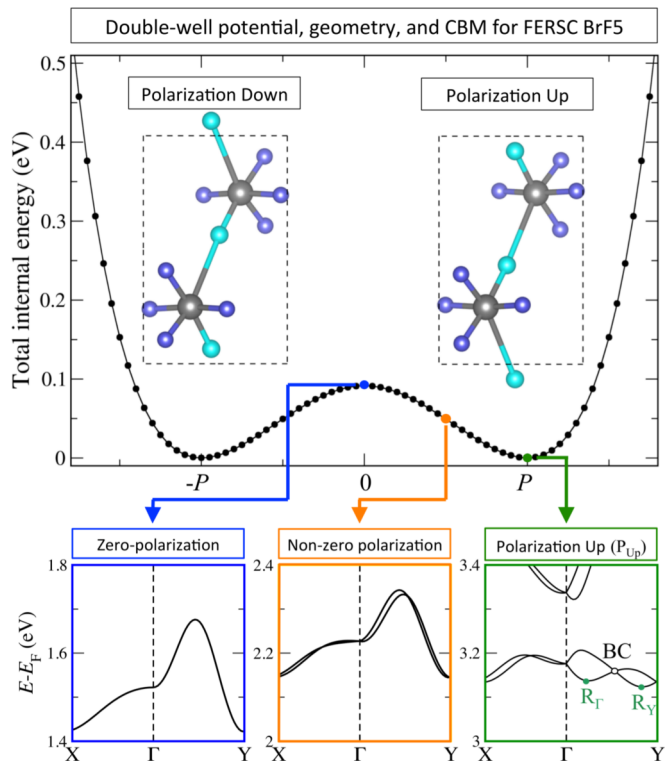


FIG. 4. Double-well potential, electrical polarized geometries, and CBM for the FERSC BrF<sub>5</sub>. The total internal energy of the ground states is taken as reference. The structures with opposite polarization directions (connected by atomic displacement) are represented in the dashed rectangle (unit cell). Br atoms are in gray and the F atoms are shown in blue. The ferroelectric active atom (F atom) is shown in cyan. For three selected points (blue, orange, and green) with zero polarization, nonzero polarization, and equilibrium polarization, the conduction band is shown in the square with the same color.

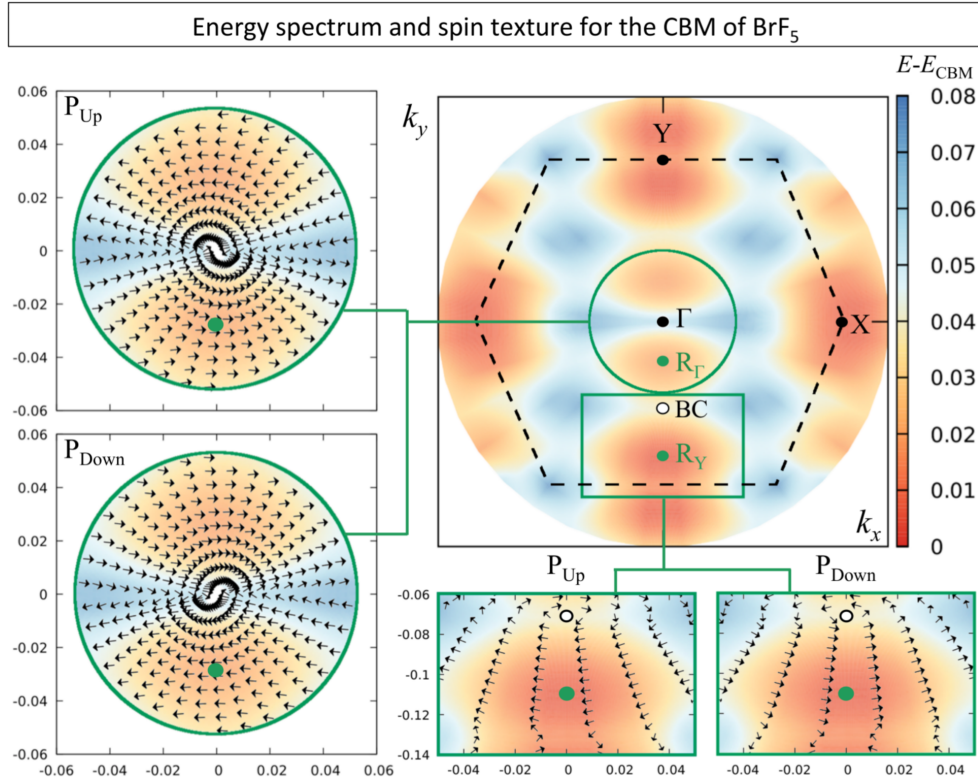


FIG. 5. Energy spectrum at the  $k_{xy}$  plane in the Brillouin zone of  $\text{BrF}_5$ . The color scale stands for the energy of the conduction bands with respect to the CBM. The energy minima along the  $\Gamma$ - $Y$  symmetry line are indicated by the green points  $R_Y$  and  $R_\Gamma$ . The band crossing (BC) along this path is also indicated by the white point. The spin texture for the polarization up and down ( $P_{\text{Up}}$  and  $P_{\text{Down}}$ ) is shown for the circular and rectangular inset.

spin splitting at the CBM of  $\approx 30$  meV with a Rashba parameter of  $0.5$  eV/Å (green square in Fig. 4). We identify two Rashba spin splittings along the  $\Gamma$ - $Y$  symmetry line, which are indicated in the band structure as  $R_\Gamma$  and  $R_Y$ . Between these RSSs, there is a band crossing (BC) indicated by the white dot. As we will show, this BC has a helical spin texture.

## 2. Transition state

When this F atom is exactly equidistant from the two Br atoms, the  $\text{BrF}_5$  space group is  $Cmcm$  (see Table II) and the compound is centrosymmetric. This fact implies that the total electric polarization is zero (blue point in the double well represented in Fig. 4). The total energy of this transition state configuration is about 80 meV/atom higher than the ground states. As expected, since the electric polarization of the transition state (TS) is zero, its energy bands are spin degenerated, which is illustrated by the CBM in Fig. 4.

## C. Confirmation of the reversal of spin texture when the FE polarization is flipped

Figure 5 shows the energy spectrum for the conduction band at the  $k_{xy}$  plane in the Brillouin zone of the FERSC  $\text{BrF}_5$ . The spin texture is shown for selected regions (indicated in green). The minimum energy for the Rashba spin splitting ( $R_\Gamma$  and  $R_Y$ ) is indicated, as well as the band-crossing point. As shown in the circular region around the  $\Gamma$  point, the spin

texture of the configuration with polarization “Up” has opposite direction to the one for the structure with polarization “Down.” This confirms the reversal spin texture expected in FERSCs.

## V. CONCLUSIONS

We establish a standard inverse design approach for the search of cofunctionalities, which is based on causal physical models and not in numerical correlations as in machine learning approaches. This strategy is then applied to the special case of stable compounds that are simultaneously ferroelectric and bulk Rashba compounds. This inverse design approach is based on the causal physical design principles for enabling the Rashba effect, ferroelectricity, and cross-functionality. In a peanut schema, we first define common DPs and unique DPs for single functionalities. The compounds having the union of these DPs are then predicted to possess cofunctionality, when the specific cofunctionality does not require additional unique conditions. This inverse design approach reveals 52 previously synthesized compounds that were not realized to be FERSC having spin splitting at the band edges. In the list of predicted compounds, 24 FERSCs are in the most stable structure (on the convex hull). Some of the found compounds have giant spin splitting, e.g.,  $\text{BrF}_5$  ( $Cmcm$ ),  $\text{TiO}_3$  ( $R3m$ ),  $\text{ZnI}_2\text{O}_6$  ( $P2_1$ ),  $\text{LaTaO}_4$  ( $Cmcm$ ),  $\text{Tl}_3\text{S}_3\text{Sb}$  ( $R3m$ ),  $\text{Sn}_2\text{P}_2\text{Se}_6$  ( $Pc$ ), and  $\text{Bi}_2\text{SiO}_5$  ( $Cmcm$ ) that have large Rashba spin splitting of 31, 57, 111, 40, 90, 67, and 76 meV, respectively.

The successful prediction of stable FERSCs with optimizing properties (e.g., Rashba bands at the band edges and small ferroelectric barrier) validates the proposed strategy. We hope that the theoretical prediction in this paper will be experimentally verified, which can open the way for future spintronic applications and the realization of devices based on the co-functionality of ferroelectricity and Rashba effect.

### ACKNOWLEDGMENTS

Work at the University of Colorado at Boulder was supported by the National Science Foundation

(NSF-DMR-CMMT Grant No. DMR-1724791). The work of G.M.D. and A.F. in Brazil was supported by the São Paulo Research Foundation FAPESP (Grant No. 17/02317-2) and by CNPq. C.M.A. is supported by FAPESP (Grants No. 18/11856-7 and No. 19/11641-0). High-throughput first-principles calculations were performed using the computational infrastructure of the LNCC supercomputer center (Santos Dumont) in Brazil. Thanks to Dr. Xiaoli Zhang for invaluable comments and discussions on design principles enabling ferroelectricity. Thanks to Dr. Oleksandr Malyi for discussion of the determination of high-symmetry centrosymmetric structures for polar structures. A.Z. thanks Emmanuel Rashba for discussions on the subject.

- 
- [1] A. Franceschetti and A. Zunger, The inverse band-structure problem of finding an atomic configuration with given electronic properties, *Nature (London)* **402**, 60 (1999).
- [2] G. E. Eperon, T. Leijtens, K. A. Bush, R. Prasanna, T. Green, J. T.-W. Wang, D. P. McMeekin, G. Volonakis, R. L. Milot, R. May, A. Palmstrom, D. J. Slotcavage, R. A. Belisle, J. B. Patel, E. S. Parrott, R. J. Sutton, W. Ma, F. Moghadam, B. Conings, A. Babayigit, H.-G. Boyen, S. Bent, F. Giustino, L. M. Herz, M. B. Johnston, M. D. McGehee, and H. J. Snaith, Perovskite-perovskite tandem photovoltaics with optimized band gaps, *Science* **354**, 861 (2016).
- [3] C. Buzea and T. Yamashita, Review of the superconducting properties of  $\text{MgB}_2$ , *Supercond. Sci. Technol.* **14**, R115 (2001).
- [4] H. Luo, M. Jain, T. M. McCleskey, E. Bauer, A. K. Burrell, and Q. Jia, Optical and structural properties of single phase epitaxial P-type transparent oxide thin films, *Adv. Mater.* **19**, 3604 (2007).
- [5] S. Curtarolo, W. Setyawan, G. L. W. Hart, M. Jahnatek, R. V. Chepulskii, R. H. Taylor, S. Wang, J. Xue, K. Yang, O. Levy, M. J. Mehl, H. T. Stokes, D. O. Demchenko, and D. Morgan, AFLOW: An automatic framework for high-throughput materials discovery, *Comput. Mater. Sci.* **58**, 218 (2012).
- [6] A. Jain, S. P. Ong, G. Hautier, W. Chen, W. D. Richards, S. Dacek, S. Cholia, D. Gunter, D. Skinner, G. Ceder, and K. A. Persson, Commentary: The materials project: A materials genome approach to accelerating materials innovation, *APL Materials* **1**, 011002 (2013).
- [7] J. E. Saal, S. Kirklin, M. Aykol, B. Meredig, and C. Wolverton, Materials design and discovery with high-throughput density functional theory: The open quantum materials database (OQMD), *JOM* **65**, 1501 (2013).
- [8] S. Kirklin, J. E. Saal, B. Meredig, A. Thompson, J. W. Doak, M. Aykol, S. Rühl, and C. Wolverton, The open quantum materials database (OQMD): Assessing the accuracy of DFT formation energies, *Npj Comput Mater* **1**, 15010 (2015).
- [9] Q. Wu, G. Autès, N. Mounet, and O. V. Yazyev, TopoMat: A database of high-throughput first-principles calculations of topological materials, *Materials Cloud Archive* 2019.0019/v1 (2019), doi: 10.24435/materialscloud:2019.0019/v1.
- [10] N. Mounet, M. Gibertini, P. Schwaller, D. Campi, A. Merkys, A. Marrazzo, T. Sohier, I. E. Castelli, A. Cepellotti, G. Pizzi, and N. Marzari, Two-dimensional materials from high-throughput computational exfoliation of experimentally known compounds, *Nature Nanotech* **13**, 246 (2018).
- [11] F. A. Rasmussen and K. S. Thygesen, Computational 2D materials database: Electronic structure of transition-metal dichalcogenides and oxides, *J. Phys. Chem. C* **119**, 13169 (2015).
- [12] F. Tang, H. C. Po, A. Vishwanath, and X. Wan, Comprehensive search for topological materials using symmetry indicators, *Nature (London)* **566**, 486 (2019).
- [13] M. G. Vergniory, L. Elcoro, C. Felser, N. Regnault, B. A. Bernevig, and Z. Wang, A complete catalogue of high-quality topological materials, *Nature (London)* **566**, 480 (2019).
- [14] T. Zhang, Y. Jiang, Z. Song, H. Huang, Y. He, Z. Fang, H. Weng, and C. Fang, Catalogue of topological electronic materials, *Nature (London)* **566**, 475 (2019).
- [15] J. W. Bennett, K. F. Garrity, K. M. Rabe, and D. Vanderbilt, Hexagonal ABC Semiconductors as Ferroelectrics, *Phys. Rev. Lett.* **109**, 167602 (2012).
- [16] K. F. Garrity, High-throughput first-principles search for new ferroelectrics, *Phys. Rev. B* **97**, 024115 (2018).
- [17] T. E. Smidt, S. A. Mack, S. E. Reyes-Lillo, A. Jain, and J. B. Neaton, An automatically curated first-principles database of ferroelectrics, *Sci. Data* **7**, 72 (2020).
- [18] G. R. Schleder, A. C. M. Padilha, C. M. Acosta, M. Costa, and A. Fazzio, From DFT to machine learning: recent approaches to materials science: A review, *J. Phys. Mater.* **2**, 032001 (2019).
- [19] C. M. Acosta, E. Ogoshi, A. Fazzio, G. M. Dalpian, and A. Zunger, The Rashba scale: Emergence of band anti-crossing as a design principle for materials with large Rashba coefficient, *Matter* **3**, 145 (2020).
- [20] M. Fiebig, T. Lottermoser, D. Meier, and M. Trassin, The evolution of multiferroics, *Nat. Rev. Mater.* **1**, 16046 (2016).
- [21] N. A. Hill, Why are there so few magnetic ferroelectrics? *J. Phys. Chem. B* **104**, 6694 (2000).
- [22] X. Zhang, L. Zhang, J. D. Perkins, and A. Zunger, Intrinsic Transparent Conductors Without Doping, *Phys. Rev. Lett.* **115**, 176602 (2015).
- [23] F. Yan, X. Zhang, Y. G. Yu, L. Yu, A. Nagaraja, T. O. Mason, and A. Zunger, Design and discovery of a novel half-Heusler transparent hole conductor made of all-metallic heavy elements, *Nat. Commun.* **6**, 7308 (2015).

- [24] G. Brunin, F. Ricci, V.-A. Ha, G.-M. Rignanese, and G. Hautier, Transparent conducting materials discovery using high-throughput computing, *Npj Comput Mater* **5**, 63 (2019).
- [25] D. G. Cahill, S. K. Watson, and R. O. Pohl, Lower limit to the thermal conductivity of disordered crystals, *Phys. Rev. B* **46**, 6131 (1992).
- [26] C. Chiritescu, D. G. Cahill, N. Nguyen, D. Johnson, A. Bodapati, P. Keblinski, and P. Zschack, Ultralow thermal conductivity in disordered, layered WSe<sub>2</sub> crystals, *Science* **315**, 351 (2007).
- [27] A. Zunger, Inverse design in search of materials with target functionalities, *Nat. Rev. Chem.* **2**, 0121 (2018).
- [28] P. Piquini, P. A. Graf, and A. Zunger, Band-Gap Design of Quaternary (In,Ga)(As,Sb) Semiconductors via the Inverse-Band-Structure Approach, *Phys. Rev. Lett.* **100**, 186403 (2008).
- [29] J. Noh, J. Kim, H. S. Stein, B. Sanchez-Lengeling, J. M. Gregoire, A. Aspuru-Guzik, and Y. Jung, Inverse design of solid-state materials via a continuous representation, *Matter* **1**, 1370 (2019).
- [30] D. Di Sante, P. Barone, R. Bertacco, and S. Picozzi, Electric control of the giant Rashba effect in bulk GeTe, *Adv. Mater.* **25**, 509 (2013).
- [31] N. Setter, D. Damjanovic, L. Eng, G. Fox, S. Gevorgian, S. Hong, A. Kingon, H. Kohlstedt, N. Y. Park, G. B. Stephenson, I. Stolichnov, A. K. TagansteV, D. V. Taylor, T. Yamada, and S. Streiffer, Ferroelectric thin films: Review of materials, properties, and applications, *J. Appl. Phys.* **100**, 051606 (2006).
- [32] H. Djani, A. C. Garcia-Castro, W.-Y. Tong, P. Barone, E. Bousquet, S. Picozzi, and P. Ghosez, Rationalizing and engineering Rashba spin-splitting in ferroelectric oxides, *Npj Quantum Mater.* **4**, 51 (2019).
- [33] L. G. D. da Silveira, P. Barone, and S. Picozzi, Rashba-Dresselhaus spin-splitting in the bulk ferroelectric oxide BiAlO<sub>3</sub>, *Phys. Rev. B* **93**, 245159 (2016).
- [34] J. Varignon, J. Santamaria, and M. Bibes, Electrically Switchable and Tunable Rashba-Type Spin Splitting in Covalent Perovskite Oxides, *Phys. Rev. Lett.* **122**, 116401 (2019).
- [35] A. Narayan, Class of Rashba ferroelectrics in hexagonal semiconductors, *Phys. Rev. B* **92**, 220101(R) (2015).
- [36] D. Di Sante, P. Barone, A. Stroppa, K. F. Garrity, D. Vanderbilt, and S. Picozzi, Intertwined Rashba, Dirac, and Weyl Fermions in Hexagonal Hyperferroelectrics, *Phys. Rev. Lett.* **117**, 076401 (2016).
- [37] M. Kim, J. Im, A. J. Freeman, J. Ihm, and H. Jin, Switchable  $S = 1/2$  and  $J = 1/2$  Rashba bands in ferroelectric halide perovskites, *Proc. Natl. Acad. Sci. USA* **111**, 6900 (2014).
- [38] K. Frohna, T. Deshpande, J. Harter, W. Peng, B. A. Barker, J. B. Neaton, S. G. Louie, O. M. Bakr, D. Hsieh, and M. Bernardi, Inversion symmetry and bulk Rashba effect in methylammonium lead iodide perovskite single crystals, *Nat. Commun.* **9**, 1829 (2018).
- [39] B. Zhou, Ferroelectric Rashba semiconductors, AgBiP X (X = S, Se and Te), with valley polarization: An avenue towards electric and nonvolatile control of spintronic devices, *Nanoscale* **12**, 5533 (2020).
- [40] R. Arras, J. Gosteau, H. J. Zhao, C. Paillard, Y. Yang, and L. Bellaiche, Rashba-like spin-orbit and strain effects in tetragonal PbTiO<sub>3</sub>, *Phys. Rev. B* **100**, 174415 (2019).
- [41] E. Plekhanov, P. Barone, D. Di Sante, and S. Picozzi, Engineering relativistic effects in ferroelectric SnTe, *Phys. Rev. B* **90**, 161108 (2014).
- [42] H. Lee, J. Im, and H. Jin, Emergence of the giant out-of-plane Rashba effect and tunable nanoscale persistent spin helix in ferroelectric SnTe thin films, *Appl. Phys. Lett.* **116**, 022411 (2020).
- [43] J. Kim, K.-W. Kim, D. Shin, S.-H. Lee, J. Sinova, N. Park, and H. Jin, Prediction of ferroelectricity-driven berry curvature enabling charge- and spin-controllable photocurrent in tin telluride monolayers, *Nat. Commun.* **10**, 3965 (2019).
- [44] A. Stroppa, D. Di Sante, P. Barone, M. Bokdam, G. Kresse, C. Franchini, M.-H. Whangbo, and S. Picozzi, Tunable ferroelectric polarization and its interplay with spin-orbit coupling in tin iodide perovskites, *Nat. Commun.* **5**, 5900 (2014).
- [45] L. L. Chang, P. J. Stiles, and L. Esaki, Electron barriers in Al-Al<sub>2</sub>O<sub>3</sub>-SnTe and Al-Al<sub>2</sub>O<sub>3</sub>-GeTe tunnel junctions, *IBM J. Res. Dev.* **10**, 484 (1966).
- [46] C. Rinaldi, S. Varotto, M. Asa, J. Sławińska, J. Fujii, G. Vinai, S. Cecchi, D. Di Sante, R. Calarco, I. Vobornik, G. Panaccione, S. Picozzi, and R. Bertacco, Ferroelectric control of the spin texture in GeTe, *Nano Lett.* **18**, 2751 (2018).
- [47] M. Liebmann, C. Rinaldi, D. Di Sante, J. Kellner, C. Pauly, R. N. Wang, J. E. Boschker, A. Giussani, S. Bertoli, M. Cantoni, L. Baldrati, M. Asa, I. Vobornik, G. Panaccione, D. Marchenko, J. Sánchez-Barriga, O. Rader, R. Calarco, S. Picozzi, R. Bertacco, and M. Morgenstern, Giant Rashba-type spin splitting in ferroelectric GeTe(111), *Adv. Mater.* **28**, 560 (2016).
- [48] I.-H. Park, Q. Zhang, K. C. Kwon, Z. Zhu, W. Yu, K. Leng, D. Giovanni, H. S. Choi, I. Abdelwahab, Q.-H. Xu, T. C. Sum, and K. P. Loh, Ferroelectricity and Rashba effect in a two-dimensional Dion-Jacobson hybrid organic-inorganic perovskite, *J. Am. Chem. Soc.* **141**, 15972 (2019).
- [49] L. Pintilie, I. Vrejoiu, D. Hesse, G. LeRhun, and M. Alexe, Ferroelectric polarization-leakage current relation in high quality epitaxial Pb(Zr, Ti)O<sub>3</sub> films, *Phys. Rev. B* **75**, 104103 (2007).
- [50] S. Picozzi, Ferroelectric Rashba semiconductors as a novel class of multifunctional materials, *Front. Phys.* **2**, 10 (2014).
- [51] Inorganic Crystal Structure Database, Crystallography, LibGuides at University of California San Diego, <https://Ucsd.Libguides.Com/Crystallography/Icsd>.
- [52] K. Ishizaka, M. S. Bahramy, H. Murakawa, M. Sakano, T. Shimojima, T. Sonobe, K. Koizumi, S. Shin, H. Miyahara, A. Kimura, K. Miyamoto, T. Okuda, H. Namatame, M. Taniguchi, R. Arita, N. Nagaosa, K. Kobayashi, Y. Murakami, R. Kumai, Y. Kaneko, Y. Onose, and Y. Tokura, Giant Rashba-type spin splitting in bulk BiTeI, *Nat. Mater.* **10**, 521 (2011).
- [53] M. S. Bahramy, R. Arita, and N. Nagaosa, Origin of giant bulk Rashba splitting: Application to BiTeI, *Phys. Rev. B* **84**, 041202(R) (2011).
- [54] X. Zhang, Q. Liu, J.-W. Luo, A. J. Freeman, and A. Zunger, Hidden spin polarization in inversion-symmetric bulk crystals, *Nat. Phys.* **10**, 387 (2014).
- [55] A. Manchon, H. C. Koo, J. Nitta, S. M. Frolov, and R. A. Duine, New perspectives for Rashba spin-orbit coupling, *Nat. Mater.* **14**, 871 (2015).

- [56] M. Sakano, J. Miyawaki, A. Chainani, Y. Takata, T. Sonobe, T. Shimojima, M. Oura, S. Shin, M. S. Bahramy, R. Arita, N. Nagaosa, H. Murakawa, Y. Kaneko, Y. Tokura, and K. Ishizaka, Three-dimensional bulk band dispersion in polar BiTeI with giant Rashba-type spin splitting, *Phys. Rev. B* **86**, 085204 (2012).
- [57] Y. Feng, Q. Jiang, B. Feng, M. Yang, T. Xu, W. Liu, X. Yang, M. Arita, E. F. Schwier, K. Shimada, H. O. Jeschke, R. Thomale, Y. Shi, X. Wu, S. Xiao, S. Qiao, and S. He, Rashba-like spin splitting along three momentum directions in trigonal layered PtBi<sub>2</sub>, *Nat. Commun.* **10**, 4765 (2019).
- [58] Y. Zhai, S. Baniya, C. Zhang, J. Li, P. Haney, C.-X. Sheng, E. Ehrenfreund, and Z. V. Vardeny, Giant Rashba splitting in 2D organic-inorganic halide perovskites measured by transient spectroscopies, *Sci. Adv.* **3**, e1700704 (2017).
- [59] S. Banik, P. K. Das, A. Bendounan, I. Vobornik, A. Arya, N. Beaulieu, J. Fujii, A. Thamizhavel, P. U. Sastry, A. K. Sinha, D. M. Phase, and S. K. Deb, Giant Rashba effect at the topological surface of PrGe revealing antiferromagnetic spintronics, *Sci. Rep.* **7**, 4120 (2017).
- [60] M. E. Lines and A. M. Glass, *Principles and Applications of Ferroelectrics and Related Materials* (Oxford University, New York, 2001).
- [61] W. Cochran, Crystal Stability and the Theory of Ferroelectricity, *Phys. Rev. Lett.* **3**, 412 (1959).
- [62] G. Burns, Dirty displacive ferroelectrics, *Phys. Rev. B* **13**, 215 (1976).
- [63] J. Valasek, Piezo-electric and allied phenomena in Rochelle salt, *Phys. Rev.* **17**, 475 (1921).
- [64] P.-P. Shi, Y.-Y. Tang, P.-F. Li, W.-Q. Liao, Z.-X. Wang, Q. Ye, and R.-G. Xiong, Symmetry breaking in molecular ferroelectrics, *Chem. Soc. Rev.* **45**, 3811 (2016).
- [65] M. Paściak, S. E. Bouffelfel, and S. Leoni, Polarized cluster dynamics at the paraelectric to ferroelectric phase transition in BaTiO<sub>3</sub>, *J. Phys. Chem. B* **114**, 16465 (2010).
- [66] M. B. Smith, K. Page, T. Siegrist, P. L. Redmond, E. C. Walter, R. Seshadri, L. E. Brus, and M. L. Steigerwald, Crystal structure and the paraelectric-to-ferroelectric phase transition of nanoscale BaTiO<sub>3</sub>, *J. Am. Chem. Soc.* **130**, 6955 (2008).
- [67] T. Nagai, Y. Mochizuki, H. Shirakuni, A. Nakano, F. Oba, I. Terasaki, and H. Taniguchi, Phase transition from weak ferroelectricity to incipient ferroelectricity in Li<sub>2</sub>Sr(Nb<sub>1-x</sub>Ta<sub>x</sub>)O, *Chem. Mater.* **32**, 744 (2020).
- [68] X.-G. Zhao, G. M. Dalpian, Z. Wang, and A. Zunger, Polymorphous nature of cubic halide perovskites, *Phys. Rev. B* **101**, 155137 (2020).
- [69] G. Trimarchi, Z. Wang, and A. Zunger, Polymorphous band structure model of gapping in the antiferromagnetic and paramagnetic phases of the Mott insulators MnO, FeO, CoO, and NiO, *Phys. Rev. B* **97**, 035107 (2018).
- [70] P. Sharma, F.-X. Xiang, D.-F. Shao, D. Zhang, E. Y. Tsymlal, A. R. Hamilton, and J. Seidel, A room-temperature ferroelectric semimetal, *Sci. Adv.* **5**, eaax5080 (2019).
- [71] N. A. Benedek and C. J. Fennie, Why are there so few perovskite ferroelectrics? *J. Phys. Chem. C* **117**, 13339 (2013).
- [72] J. Krempaský, S. Muff, J. Minár, N. Pilet, M. Fanciulli, A. P. Weber, E. B. Guedes, M. Caputo, E. Müller, V. V. Volobuev, M. Gmitra, C. A. F. Vaz, V. Scagnoli, G. Springholz, and J. H. Dil, Operando imaging of all-electric spin texture manipulation in ferroelectric and multiferroic Rashba semiconductors, *Phys. Rev. X* **8**, 021067 (2018).
- [73] I. Žutić, J. Fabian, and S. Das Sarma, Spintronics: Fundamentals and applications, *Rev. Mod. Phys.* **76**, 323 (2004).
- [74] E. I. Rashba, Properties of semiconductors with an extremum loop. I. Cyclotron and combinational resonance in a magnetic field perpendicular to the plane of the loop, *Sov. Phys. Solid State* **2**, 1109 (1960).
- [75] W. C. Martin, Table of spin-orbit energies for p-electrons in neutral atomic (Core) Np configurations, *J. Res. Nat. Bur. Stand. Sect. A* **75A**, 109 (1971).
- [76] H. Nakamura, T. Koga, and T. Kimura, Experimental Evidence of Cubic Rashba Effect in an Inversion-Symmetric Oxide, *Phys. Rev. Lett.* **108**, 206601 (2012).
- [77] Sz. Vajna, E. Simon, A. Szilva, K. Palotas, B. Ujfalussy, and L. Szunyogh, Higher-order contributions to the Rashba-Bychkov effect with application to the Bi/Ag(111) surface alloy, *Phys. Rev. B* **85**, 075404 (2012).
- [78] S. P. Ong, W. D. Richards, A. Jain, G. Hautier, M. Kocher, S. Cholia, D. Gunter, V. L. Chevrier, K. A. Persson, and G. Ceder, Python materials genomics (Pymatgen): A robust, open-source python library for materials analysis, *Comput. Mater. Sci.* **68**, 314 (2013).
- [79] J. P. Perdew, K. Burke, and M. Ernzerhof, Generalized Gradient Approximation Made Simple, *Phys. Rev. Lett.* **77**, 3865 (1996).
- [80] A. I. Liechtenstein, V. I. Anisimov, and J. Zaanen, Density-functional theory and strong interactions: Orbital ordering in Mott-Hubbard insulators, *Phys. Rev. B* **52**, R5467 (1995).
- [81] G. Kresse and J. Furthmüller, Efficient iterative schemes for *ab initio* total-energy calculations using a plane-wave basis set, *Phys. Rev. B* **54**, 11169 (1996).
- [82] G. Kresse and D. Joubert, From ultrasoft pseudopotentials to the projector augmented-wave method, *Phys. Rev. B* **59**, 1758 (1999).
- [83] T. Chattopadhyay, J. X. Boucherle, and H. G. von Schnering, Neutron diffraction study on the structural phase transition in GeTe, *J. Phys. C* **20**, 1431 (1987).
- [84] A. Olsen, P. Goodman, and H. J. Whitfield, The Structure Tl<sub>3</sub>SbS<sub>3</sub>, Tl<sub>3</sub>SbSe<sub>3</sub>, Tl<sub>3</sub>SbS<sub>3-x</sub>Se<sub>x</sub>, and Tl<sub>3</sub>Sb<sub>y</sub>As<sub>1-y</sub>Se<sub>3</sub>, *J. Solid State Chem.* **60**, 305 (1985).
- [85] R. Israëel, R. de Gelder, J. M. M. Smits, P. T. Beurskens, S. W. H. Eijt, Th. Rasing, H. van Kempen, M. M. Maior, and S. F. Motrija, Crystal structures of Di-tin-hexa(seleno)hypodiphosphate, Sn<sub>2</sub>P<sub>2</sub>Se<sub>6</sub>, in the ferroelectric and paraelectric phase, *Zeitschrift Für Kristallographie, Crystalline Materials* **213**, 34 (1998).
- [86] J. G. Bergman and J. S. Wood, Structure of thallium(I) iodate, *Acta Crystallogr. Sect. C* **43**, 1831 (1987).
- [87] Y. Yang, P. Brazis, C. R. Kannewurf, and J. A. Ibers, Structures and conductivities of the quaternary A/Bi/Cu/S phases KBi<sub>2</sub>CuS<sub>4</sub> and A<sub>3</sub>Bi<sub>5</sub>Cu<sub>2</sub>S<sub>10</sub> (A = Rb, Cs), *J. Solid State Chem.* **155**, 243 (2000).
- [88] H. M. McConnell, Theory of nuclear magnetic shielding in molecules. I. Long-range dipolar shielding of protons, *J. Chem. Phys.* **27**, 226 (1957).
- [89] B. G. Mueller and M. Serafin, ChemInform abstract: Single-crystal investigations on PtF<sub>4</sub> and PtF<sub>5</sub>, *ChemInform* **23** (2010), doi: 10.1002/chin.199245006.

- [90] G. Thiele, H. W. Rotter, and K. D. Schmidt, Kristallstrukturen und phasentransformationen von caesiumtrihalogenogermanaten(II) CsGeX<sub>3</sub> (X = Cl, Br, I), *Z. Anorg. Allg. Chem.* **545**, 148 (1987).
- [91] P. Bottcher, Darstellung und kristallstruktur der dialkalimetalltrichalkogenide Rb<sub>2</sub>S<sub>3</sub>, Rb<sub>2</sub>Se<sub>3</sub>, Cs<sub>2</sub>S<sub>3</sub> und Cs<sub>2</sub>Se<sub>3</sub>, *Z. Anorg. Allg. Chem.* **461**, 13 (1980).
- [92] S. C. Abrahams, H. J. Levinstein, and J. M. Reddy, Ferroelectric lithium niobate. 5. Polycrystal x-ray diffraction study between 24° and 1200 °C, *J. Phys. Chem. Solids* **27**, 1019 (1966).
- [93] H. D. Rad and R. Hoppe, Über thiomercurate. 3. Zur Kenntnis von Ba[HgS<sub>2</sub>], *Z. Anorg. Allg. Chem.* **483**, 18 (1981).
- [94] H. Y.-P. Hong, J. C. Mikkelsen, and G. W. Roland, Crystal structure of Tl<sub>3</sub>AsSe<sub>3</sub>, *Mater. Res. Bull.* **9**, 365 (1974).
- [95] K. A. Chuntunov, A. N. Orlov, S. P. Yatsenko, Yu. N. Grin', and L. D. Miroshnikova, Synthesis of chalcogenides of A<sub>21</sub>B<sub>36</sub> composition and crystalline structure of Rb<sub>2</sub>Te<sub>3</sub> and Cs<sub>2</sub>Te<sub>3</sub>, *Izv. Akad. Nauk. SSSR, Neorg. Mater. [Inorg. Mater. (USSR)]* **18**, 1113 (1982).
- [96] J. Galy and R. Enjalbert, Crystal chemistry of the VA element trihalides: Lone pair, stereochemistry, and structural relationships, *J. Solid State Chem.* **44**, 1 (1982).
- [97] F. Pertlik, Crystal structure of Ag<sub>2</sub>TeS<sub>3</sub> and Na(Na<sub>1-x</sub>Ag<sub>x</sub>)TeS<sub>3</sub> (x ≈ 0.5) and the geometry of Te(IV)S<sub>3</sub> polyhedra, *Monatsh. Chem.* **128**, 157 (1997).
- [98] H.-L. Keller and L. Wimbart, Über münzmetall-quecksilberchalkogenidhalogenide. III Zur kristallstruktur von Ag<sub>2</sub>HgSI<sub>2</sub>, *Z. Anorg. Allg. Chem.* **629**, 2337 (2003).
- [99] F. Emmerling, D. Petri, and C. Rohr, Neue arsenide mit As-Ketten und -Ringen: BaAs<sub>2</sub> und AlBa<sub>2</sub>As<sub>5</sub> (Al = K, Rb), *Z. Anorg. Allg. Chem.* **630**, 2490 (2004).
- [100] P. Berastegui, S. Hull, and S.-G. Eriksson, A low-temperature structural phase transition in CsPbF<sub>3</sub>, *J. Phys.: Condens. Matter* **13**, 5077 (2001).
- [101] P. Wu and J. A. Ibers, Synthesis and structures of the quaternary chalcogenides of the Type KLnMQ<sub>4</sub> (Ln = La, Nd, Gd, Y; M = Si, Ge; Q = S, Se), *J. Solid State Chem.* **107**, 347 (1993).
- [102] J. Lapasset, H. N. Bordallo, R. Almairac, and J. Nouet, Redetermination of the crystal structure of barium tetrafluorozincate, BaZnF<sub>4</sub>, at 295 K and 113 K, *Zeitschrift Für Kristallographie, Crystalline Materials* **211**, 934 (1996).
- [103] B. C. Chan and P. K. Dorhout, Crystal structures of potassium terbium(III) tetrasulfidogermanate, K<sub>2</sub>TbGeS<sub>4</sub>, and potassium praseodymium(III) tetraselenidogermanate, K<sub>2</sub>PrGeSe<sub>4</sub>, *Zeitschrift Für Kristallographie, New Crystal Structures* **220**, 7 (2005).
- [104] J. C. Dewan and A. J. Edwards, Fluoride crystal structures. Part 27. Seleninyl difluoride at -35 °C, *J. Chem. Soc., Dalton Trans.* **23**, 2433 (1976).
- [105] F. S. Liu, Q. L. Liu, J. K. Liang, L. T. Yang, G. B. Song, J. Luo, and G. H. Rao, A systematic study on crystal structure and magnetic properties of Ln<sub>3</sub>GaO<sub>6</sub> (Ln = Nd, Sm, Eu, Gd, Tb, Dy, Ho and Er), *J. Solid State Chem.* **177**, 1796 (2004).
- [106] H. D. Lutz, W. Buchmeier, E. Alici, and W. Eckers, Röntgenographische und schwingungsspektroskopische Untersuchungen an wasserfreien Chloraten und Bromaten des Strontiums, Bariums und Bleis. Kristallstruktur des Sr(ClO<sub>3</sub>)<sub>2</sub> und Sr(BrO<sub>3</sub>)<sub>2</sub>, *Z. Anorg. Allg. Chem.* **529**, 46 (1985).
- [107] J. Ketterer and V. Kramer, Crystal structure of the bismuth silicate Bi<sub>2</sub>SiO<sub>5</sub>, *neues jahrbuch fur mineralogie, Monatshefte* **01**, 13 (1986).
- [108] R. J. Finch, M. A. Cooper, A. C. Hawthorne, and R. C. Ewing, Refinement of the crystal structure of rutherfordine, *The Canadian Mineralogist* **37**, 929 (1999).
- [109] A. A. Belik, T. Wuernisha, T. Kamiyama, K. Mori, M. Maie, T. Nagai, Y. Matsui, and E. Takayama-Muromachi, High-pressure synthesis, crystal structures, and properties of perovskite-like BiAlO<sub>3</sub> and pyroxene-like BiGaO<sub>3</sub>, *Chem. Mater.* **18**, 133 (2006).
- [110] B. Ribár and W. Nowacki, Die kristallstruktur von stephanit, [SbS<sub>3</sub>]S[Ag<sub>5</sub>III], *Acta Crystallogr. Sect. B* **26**, 201 (1970).
- [111] I. P. Zibrov, V. P. Filonenko, M. Sundberg, and P.-E. Werner, Structures and phase transitions of B-Ta<sub>2</sub>O<sub>5</sub> and Z-Ta<sub>2</sub>O<sub>5</sub>: Two high-pressure forms of Ta<sub>2</sub>O<sub>5</sub>, *Acta Crystallogr. Sect. B* **56**, 659 (2000).
- [112] M. Gostojić, Die kristallstruktur von synthetischem elisit, Tl<sub>3</sub>AsS<sub>3</sub>\*, *Zeitschrift Für Kristallographie, Crystalline Materials* **151**, 249 (1980).
- [113] F. Gingl, BaMgF<sub>4</sub> and Ba<sub>2</sub>Mg<sub>3</sub>F<sub>10</sub>: New examples for structural relationships between hydrides and fluorides, *Z. Anorg. Allg. Chem.* **623**, 705 (1997).
- [114] H. Kasatani, S. Aoyagi, Y. Kuroiwa, K. Yagi, R. Katayama, and H. Terauchi, Study of crystal structure at high temperature phase in KIO<sub>3</sub> crystal by synchrotron powder x-ray diffraction, *Nucl. Instrum. Methods Phys. Res., B* **199**, 49 (2003).
- [115] H. Wozzala and K. H. Jost, Die kristallstruktur des bleimonohydrogentriphosphats, Pb<sub>2</sub>HP<sub>3</sub>O<sub>10</sub>, *Z. Anorg. Allg. Chem.* **445**, 36 (1978).
- [116] J. D. Grice, A solution to the crystal structures of bismutite and beyerite, *The Canadian Mineralogist* **40**, 693 (2002).
- [117] H. Bartl, Meßzeitersparnis durch profilauswertung bei der registrierung von neutroneneinkristallreflexen: Die kristallstruktur von wismuttrichlorid, BiCl<sub>3</sub>, *Z. Anal. Chem.* **312**, 17 (1982).
- [118] R. Liminga, C. Svensson, J. Albertsson, and S. C. Abrahams, Gamma-lithium iodate structure at 515 K and the A-LiIO<sub>3</sub> to Γ-LiIO<sub>3</sub>, to B-LiIO<sub>3</sub> phase transitions, *J. Chem. Phys.* **77**, 4222 (1982).
- [119] H. Effenberger, Structure investigations of Tl(I)-arsenates(V): Tl<sub>3</sub>(AsO<sub>4</sub>), Tl<sub>2</sub>Cu(I)(AsO<sub>4</sub>) and TlCu(II)<sub>2</sub>(AsO<sub>4</sub>)(AsO<sub>3</sub>OH), *Zeitschrift Für Kristallographie, Crystalline Materials* **213**, 42 (1998).
- [120] M. Avdeev and V. Kharton, Crystal structure of rhombohedral MCd(NO<sub>2</sub>)<sub>3</sub> [M = KRb, Cs, Tl] from x-ray powder diffraction data, *Mater. Res. Bull.* **37**, 735 (2002).
- [121] J.-K. Liang and C.-G. Wang, The structure of Zn (I O<sub>3</sub>)<sub>2</sub> Crystal, *Huaxue Xuebao* **40**, 985 (1982).
- [122] P. Bayliss, Crystal chemistry and crystallography of some minerals within the pyrite group, *American Mineralogist* **74**, 1168 (1989).

- [123] R. Gerardin, Preparation and identification of a new ternary compound, lithium beryllium antimonide (Li Be Sb), *C. R. Acad. Sci. Ser. C* **284**, 679 (1977).
- [124] Ž. P. Čančarević, J. C. Schön, and M. Jansen, Possible existence of alkali metal orthocarbonates at high pressure, *Chem. Eur. J.* **13**, 7330 (2007).
- [125] D. Zagorac, K. Doll, J. C. Schön, and M. Jansen, *Ab initio* structure prediction for lead sulfide at standard and elevated pressures, *Phys. Rev. B* **84**, 045206 (2011).
- [126] J.-Q. Dai and Z. Fang, Structural, electronic, and polarization properties of  $\text{Bi}_2\text{ZnTiO}_6$  supercell from first-principles, *J. Appl. Phys.* **111**, 114101 (2012).
- [127] S. Ju and G.-Y. Guo, First-principles study of crystal structure, electronic structure, and second-harmonic generation in a polar double perovskite  $\text{Bi}_2\text{ZnTiO}_6$ , *J. Chem. Phys.* **129**, 194704 (2008).
- [128] S. Kashida, Electronic structure of  $\text{Ag}_2\text{S}$ , band calculation and photoelectron spectroscopy, *Solid State Ionics* **158**, 167 (2003).